SPRINGTIME FLOODING DYNAMICS IN THE UPPER WOLASTOQ BASIN BASED ON REGIONAL CLIMATE MODEL SIMULATIONS

by

Ahmed Shalaby

PhD, Cairo University, 2012

A Thesis Submitted in Partial Fulfillment
of the Requirements for the Degree of

Master of Science in Forestry

in the Graduate Academic Unit of Forestry and Environmental Management

Supervisor: Charles P. A. Bourque, PhD, Forestry and Environmental Management

Examining Board: Paul A. Arp, PhD, Forestry and Environmental Management, Chair
Siddharth Raval, PhD, Department of Mechanical Engineering,
Zisheng Xing, PhD, Agriculture and Agri-Food Canada

This thesis is accepted by the
Dean of Graduate Studies

THE UNIVERSITY OF NEW BRUNSWICK

June, 2022

ABSTRACT

Spring flooding of the upper Wolastoq (Saint John River) basin, northeastern North America, poses a significant threat to present and future socio-economic development in the area. The spring floods of 2008 and 2018 were two of the more devastating 100-year floods affecting the basin in the past century. The objective of this study was to investigate flooding trends in the Wolastoq by tracking the daily evolution of hydroclimatic variables (e.g., air temperature, precipitation, snow accumulation, snowmelt patterns, surface runoff) and waterflow dynamics in the river from 2007–2019 based on an implementation of a regional climate model, namely RegCM4. The model's simulation provided reasonable fidelity in identifying the precise timing and magnitude of both the 2008 and 2018 flooding events. The impacts of forest-cover removal on the Wolastoq discharge rates were also examined. The surface landcover in model simulations was digitally altered from forests to agricultural lands (crops + irrigated lands) in emulating annual forest-cover removal and accumulation for 2008 and 2018. The study indicated that cumulative annual forest disturbance in the upper basin based on % forest-cover removal rates defined by Global Forest Watch products, tended to increase spring's peak discharge rates in the upper Wolastoq from 27% in 2008 to 55% in 2018.

DEDICATION

To the Wolastoq

ACKNOWLEDGMENTS

To Dr. Charles P.-A. Bourque, who opened his door to a stranger, who guided me through one of my difficult times in my life's journey. Without him, this work would not have seen the light of day. His gentle and friendly support provided peace of mind and encouragement to tackle a challenging scientific problem. Thank you for being more than just a professor, but also a mentor, motivator, and friend. Equally, I would like to offer my appreciation to my advisory committee members, Dr.'s Paul Arp and Fan-Rui Meng, for their early guidance in this project. Special thanks go to (i) Environment and Climate Change Canada (Project No. GCXE21P014) and (ii) Natural and Science and Engineering Council of Canada (NSERC) for funding this project. I am also highly grateful to the Faculty of Forestry and Environmental Management, University of New Brunswick, for providing me much appreciated financial support in the form of graduate teaching and research assistantships, and Compute Canada for making high performance computing facilities accessible to me free of charge. Finally, to Noha, my wife for more than two decades, who helped navigate our family in dark and dangerous times. Without her wisdom and infinite patience, I could not have found the strength to continue.

Table of Contents

ABSTRACT ii

Table of Contents v

List of Tables vii

List of Figures viii

Chapter 1 1

Introduction 1

1.1 Setting 1

1.2 Prediction of springtime flooding 5

1.3 The Problem 7

1.4 Thesis Structure 9

Chapter 2 10

Methods and Materials 10

2.1 RegCM4 description and simulation design 10

2.2 Snow parameterisation 15

2.3 Landcover change sensitivity experiment 17

2.4 Datasets and statistical analysis 21

Chapter 3 25

Results and Discussion 25

3.1 New Brunswick climatology and model validation 25

3.2 Spring flooding of 2008 31

3.3 Landcover change impact 39

Chapter 4 45

Conclusions 45

References 46

Vita

List of Tables

Table 1. Upper Wolastoq basin annual cumulative forest-removal; third and fourth columns represent the total within subbasin forest-area harvested (in km^2) and current year and cumulative % removal (in brackets) from 2001 to 2008 (column three) and from 2001 to 2018 (column four), respectively. 18

Table 2. Representative climate stations within Maritime Canada. 24

Table 3. Freezing and snow degree-days, i.e., FDD and SDD, respectively; FDD is calculated for the November–April snow accumulation period, whereas SDD is calculated for the March–May snowmelt period of each year from 2007–2019. 39

Table 4. Landcover-related parameters and their assigned values for both the landcover control (CTL) and landcover change experiments (LU)..... 40

List of Figures

Figure 1. B-staggered horizontal grid, with Δx and Δy representing the horizontal resolutions in both the *x* and *y* direction. **11**

Figure 2. Schematic of the terrain-following coordinate system.. ..... **12**

Figure 3. Computational domain.. ..... **14**

Figure 4. Landcover categories **15**

Figure 5. (a) Upper Wolastoq basin and its eight large subbasins. (b) The cumulative annual forest-cover loss in % of subbasin areas from 2001–2018..... **19**

Figure 6. Landcover change in the upper Wolastoq basin. (a) The landcover for the control run (CTL) (b) and (c) cumulative annual forest-cover loss from 2001–2008 and 2001–2018 (LU), respectively. **20**

Figure 7. Observed and modelled (a) monthly mean, maximum, and minimum air temperatures and (b) total precipitation at St. Pamphile, QC.. ..... **26**

Figure 8. Observed and modelled (a) monthly mean, maximum, and minimum air temperatures and (b) total precipitation at Fredericton, NB. **28**

Figure 9 Taylor diagrams of daily (a) mean, (b) maximum, (c) minimum air temperatures, and (d) total precipitation for 11 stations in the upper Wolastoq basin. The data are representative of the 2007–2019 simulation period. Colours coincide with season (legend) and the stations are ordered from north to south. **30**

Figure 10. Modelled monthly anomalies of on-the-ground snow water equivalent (SWE), snowmelt, and surface runoff for January (J), February (F), March (M), and April (A) of 2008..... **32**

Figure 11. Modelled monthly anomalies of total precipitation..... **33**

Figure 12. Modelled monthly anomalies of on-the-ground snow. **34**

Figure 13. Modelled monthly anomalies of snowmelt. **35**

Figure 14. Modelled monthly anomalies of sublimation/evaporation. **36**

Figure 15. Modelled monthly anomalies of surface runoff. **37**

Figure 16. Changes in on-the-ground snow. **41**

Figure 17. Changes in snowmelt. **42**

Figure 18. Changes in surface runoff. **43**

Figure 19. Cumulative surface runoff. **44**

Chapter 1

Introduction

In April 2008, the Wolastoq (Saint John River) basin suffered from a severe and rare flooding event. The river's stage level reached 8.35 m in proximity to Fredericton, the worst in the previous 35 years. The Wolastoq discharge rate reached 10,194 $m^3 s^{-1}$, 20 times the mean rate. Most communities along the Wolastoq, from Edmundston in the upper basin to Quispamsis near the mouth of the river, experienced severe property damage, including damage to roads, railways, homes, farms, and small businesses (Newton and Burrell, 2015). The estimated damage from that event exceeded $23 million CAD.

1.1 Setting

Spring flooding of the Wolastoq creates a major challenge for many communities in New Brunswick (NB), because of the many complications associated with forecasting such misfortunes with high fidelity. Scientific and engineering efforts to understand the processes that support flooding along the Wolastoq has a history that goes back as far as the 1960's. Most efforts to date have concentrated on collecting hydrometric and hydrometeorological data for the development of statistical models in predicting the timing and magnitude of seasonal flooding each year (El-Jabi and Caissie, 2019; Zadeh et al., 2020).

The Wolastoq is the second longest river in Atlantic Canada, after the Saint Lawrence River, and the longest in NB with a total distance of 673 km. The Wolastoq headwaters are in the Notre Dame Mountains of northern Maine (ME), USA – the farthest northern

extension of the Appalachian Mountains in eastern North America. The river flows in the northwestern part of NB and turns to the south, still in NB, to flow to the Bay of Fundy at the city of Saint John (Burrell and Anderson, 1991; Kidd et al., 2011; Newton and Burrell, 2015). The Wolastoq basin comprises three main subbasins, the upper basin (i.e., upstream of Grand Falls), the middle basin (Grand Falls to Mactaquac), and the lower basin downstream of Mactaquac (Newton and Burrell, 2015). The largest drainage area of the Wolastoq basin is at Fort Kent (ME, USA) at 14,700 km^2, Grand Falls (NB) at 21,900 km^2, East Florenceville at 34,200 km^2, and below Mactaquac at 39,900 km^2 (Aucoin et al., 2011).

The regional vegetation cover determines the dominant ecosystems in the basin. The NB Ecological Land Classification (NB ELC) divides the Wolastoq basin into seven distinct ecoregions (Kidd et al., 2011). The upper Wolastoq basin spans two of these ecoregions, the Appalachians and northern NB Highlands. The upper Wolastoq basin is covered largely with hardwood trees, e.g., sugar maple (*Acer Saccharum* Marsh.) and yellow birch (*Betula alleghaniensis* Britton; Farrar, 1995). The middle basin, which has reduced topographic relief, is covered with coniferous forests, whereas the wetland portions of the basin are resident to eastern white cedar (*Thuja occidentalis* L.) and black spruce [*Picea mariana* (Mill.) Britton, Sterns and Poggenb; Farrar, 1995]. The lower basin maintains more wetlands than the middle, offering critical habitat for basswood (*Tilia americana* L.), white ash (*Fraxinus americana* L.), and green ash (*Fraxinus pennsylvanica* Marsh.; Farrar, 1995; Kidd et al., 2011).

Atlantic Canada's current climate is characterized by cold winters, with temperatures generally below 0º C, warm summers, with a mean temperature range of 10–22ºC, and

mostly wet all year. It is characterized by a *Dfb* climatic zone, after the Köppen-Geiger climatological convention (Peel et al., 2007; Ahrens et al., 2016). New Brunswick is primarily influenced by continental Arctic airmasses in winter (i.e., cA) and maritime Atlantic airmasses in summer (mT). It is characterized by the influence of mid-latitude cyclones that impact Atlantic Canada, which are known as east-coast storms or colloquially, as nor'easters. They are intense storms that undergo cyclogenesis further south along the eastern coast of the USA and travel northeastward to eastern Canada. They gain their energy from large temperature gradients between the warm Atlantic Ocean and the cold continental landmass to the west. The water vapour supply from the warm Gulf Stream adds additional energy to these systems through the phase change of water vapour by condensation. The strength of these storms usually surpasses that of tropical storms. These storms can affect Atlantic Canada in any season of the year, from fall through spring. These storms usually bring uncharacteristic amounts of precipitation (snow, rain, or mixtures thereof) to the region (Ahrens et al., 2016).

Key elements controlling hydrometeorological processes of flooding in the Wolastoq basin are (1) topography, (2) vegetation cover and associated landuse practices, and (3) local-to-regional weather. Extreme flooding events may be attributed to multi-factor interactions at various spatiotemporal scales, and as a result flooding cannot be studied entirely by analyzing field observations alone. The study of extreme hydrological events is essential for water resource and river management, as well as agriculture and fisheries management (Aucoin et al., 2011). Spring flooding may be the result of individual processes or combinations of these processes. Some of these processes may include:

1. Melting of anomalous winter snowpacks (nival processes);

2. Intense rainfall associated with extratropical cyclones (pluvial processes);
3. Fast snowmelt rates associated with abnormally high spring air temperatures, and correspondingly high cumulative snow degree-days (SDD); and/or
4. Ice jams.

Each factor is characterized by its spatiotemporal scale and hydrometeorological processes associated with it. Flooding due to nival processes is prolonged and occurs mostly in the upper and middle subbasins of the Wolastoq. Anomalous snowpacks that may develop from late fall (i.e., November–December) to early spring (typically, mid- to late March) provides the preconditioning for anticipated late spring flooding that may last for several weeks (Collins et al., 2014). However, high-volume rainfall events associated with hurricanes and extratropical cyclones can promote pluvial processes of flooding, which may result in high-volume surface runoff over several days. Rain-on-snow events can contribute to the intensification of flooding. Rainfall in late spring can enhance the production of meltwater by transferring sensible energy, if warm enough, to melt the snowpack. The latent heat released due to condensation of ambient water vapour acts as an additional source of energy in the production of meltwater. Associated with this process is an intermediate timescale to that of purely snowmelt-generated and pluvial inputs (Collins et al., 2014).

Flooding from ice jams has recently attracted much attention in the scientific community because of its complexity, and its dependency on whether basins are regulated or unregulated (Rokaya et al., 2018). For instance, Beltaos (2002) investigated the role of ice breakup in the Wolastoq triggered by mid-winter and early spring thaws. Ice breakup was shown to increase the extent of ice jams in the river and, thus, the probability of

flooding. The study concluded that winter ice breakup could increase in the future with warming of the regional climate. A recent study by Rokaya et al. (2018) examined the impact of global warming on flooding trends initiated from ice jams, and concluded that late-winter and springtime waterflow in small, unregulated basins could be amplified due to more frequent episodes of mid-winter thaw and associated formation of ice jams. This is especially relevant to NB, where small, unregulated basins are expected to undergo significant shifts in late-winter discharge rates because of atmospheric warming.

1.2 Prediction of springtime flooding

Conventional statistical models are computationally efficient and easy to implement in modelling flooding. These models generally comply with river-engineering standards (Aucoin et al., 2011; Caissie and Robichaud, 2009; Zahmatkesh et al., 2019). Many of these statistical models are based on probability distribution functions fitted to long-term observations of river discharge rates and stage heights, with normally more than 15 years of observations. Generalized extreme value distribution functions and three-moment log-normal distributions are effective at evaluating probabilities of timing, frequency, and magnitude of daily discharge rates. Regression relations are also widely used in relating seasonal precipitation and drainage basin area as predictors of outlet-specific discharge rates (Aucoin et al., 2011; Caissie and Robichaud, 2009).

Despite their usefulness, statistical models also have their disadvantages. Firstly, they are watershed-scale dependent, and because of their design cannot easily address interactions with neighboring watersheds. Secondly, they cannot provide a mechanistic, processes-based understanding of the complexities of flooding, due to flooding's nonlinear

behaviour. Also, because of the need for historical data in their construction (Zadeh et al., 2020), the methods cannot be used to answer questions of impact associated with future climate change.

Hydrometeorological or hydroclimate models are the best means to provide such mechanistic understanding. They are utilized to perform all kinds of sensitivity analyses, and they provide the only means for projecting the impact of climate change on future flooding trends. Hydrometeorological models couple atmospheric, hydrodynamic, and land surface processes under a single unifying structure. The coupled system is formulated to address both positive and negative feedback among its various components. The value-added in using coupled models of regional climate in the study of floods and their occurrence, include making available:

1. Online calculations of hydrometeorological variables (e.g., air temperature, precipitation, surface runoff, seasonal snowmelt production, snow evaporation and sublimation, etc.) at sub-daily intervals;
2. High resolution, cloud-resolving scales < 10 km;
3. Sensitivity studies, such as investigating the impact of landcover change on climate; and
4. High-resolution regional climate projections (≤ 5-km resolution) for both historical and future time horizons.

Flood timing, frequency, and magnitude become particularly important for sustainable planning under climate change (Eljabi et al., 2015; Zadeh et al., 2020). Coupled climate models are valuable in the study of flooding dynamics associated with past and future changes in climate and land-surface conditions.

1.3 The Problem

Anthropogenic and natural deforestation impact hydroclimatic processes. These interrelations among landcover and hydrometeorological and climatic factors have long been recognized (e.g., Hibbert, 1967). Forest-cover removal has been shown in some instances to increase basin water yields and, thus, stream and river flow discharge rates. Watershed-response time to forest-cover removal can occur at least one year after disturbance, yet there still remains some degree of uncertainty (Hibbert, 1967). Many subsequent studies have validated the relationship between forest-cover removal and stream and river flow. Recently Goeking and Tarboton (2020) surveyed 78 scientific articles on this topic, written over nineteen years from 2000–2018. Many of these studies focused on snow and snowmelt processes in western and southwestern North America. Springtime streamflow in snow-dominated basins was shown to be largely controlled by differences between snowfall and sublimation of canopy-intercepted snow. Forest-cover reductions may lead to reduction in canopy-intercepted snow, reductions in evaporation of previously melted snow and sublimation of canopy snow resulting in an increase of on-the-ground accumulation of snow and subsequent increases in streamflow during the snowmelt season (Goeking and Tarboton, 2020).

Climatic impacts of forest-cover change have been studied using the International Centre of Theoretical Physics Regional Climate Model *ver.* 4 (ICTP–RegCM4, or RegCM4 in short; Giorgi et al., 2012) for many regions globally. For instance, the large, forested areas of the Great Horn of Africa have undergone gradual conversion to agricultural land over a period of about 15 years. For this landuse scenario, RegCM4 simulated a statistically significant reduction in local precipitation because of landcover

conversion and a resulting positional shift in the intertropical convergence zone (ITCZ; Otieno and Anyah, 2012). Recently, LIopart et al. (2018) studied the climatic impact of forest-cover change in the Amazonian basin with RegCM4. This research emphasised the large-scale dynamic response to such land-surface disturbance that resulted in a reduction in rainfall over the western part of the basin due to a reduction in evapotranspiration (Llopart et al., 2018). As an interesting counterintuitive example, RegCM4-generated simulations of the climatic impact of deforestation, Chen et al. (2019) showed that cumulative deforestation in the Maritime Belt of Indonesia, Philippines, and Papua New Guinea increased regional precipitation because of the development of a strong, upward synoptic-scale transport of water vapour. RegCM4 was also used to simulate the impact of future landcover change (forest to grass cover) under future warming conditions in eastern Asia (Niu et al., 2018). This work showed that under a representative concentration pathway (RCP) of 4.5, landcover change could conceivably contribute to more than 10% of the total projected warming in the area. At more localised scales, this landcover change could contribute to warming by as much as 30%.

Commercial and non-commercial forest-cover removal in eastern North America, especially in the upper Wolastoq basin, can lead to significant changes in (i) local weather patterns; (ii) snow spatiotemporal distribution; (iii) snowmelt processes; and (iv) basin hydraulic response (Yu and Bourque, 2022). The central hypothesis of this study is that the cumulative forest-cover loss in the upper Wolastoq basin can influence flooding intensity and occurrence as observed in many basins across North America. To test this hypothesis, a series of RegCM4-based simulations were created and subsequently studied. The specific research questions associated with this project involve:

1. How does RegCM4 track snowfall and snowmelt processes from 2007–2019?
2. What are the physical processes that led to the 2008 and 2018 flooding events?
3. What impacts do recurring forest-cover removal have on the hydrometeorology in the upper Wolastoq basin, including system feedback, and mid-winter to late-spring waterflow dynamics?

This study has two main objectives, namely to: (i) summarise flooding events in the upper Wolastoq by conducting continuous RegCM4-model simulations over a 12-year period from 2007–2019; and (ii) test the hypothesis that repeated forest-cover removal has a quantifiable impact on springtime waterflow and flooding dynamics in the upper Wolastoq.

1.4 Thesis Structure

Following this introductory chapter, Chapter 2 gives the methods and description of the various data sources used in regional climate model calibration and validation, and in the parametrisation of landcover change from 2007–2019. It also gives a comprehensive description of RegCM4, including elements of precipitation and snowmelt parameterisation, and modelling experiments employed in the study of landcover change effects on flooding trends in the region. It also introduces the statistical tools used in model validation. Chapter 3 introduces and discusses the results of model validation for a significant part of Maritime Canada, placing a particular focus on waterflow dynamics associated with the 2008 and 2018 springtime flooding of the upper Wolastoq. Also addressed are the impacts of repeated forest-cover removal on springtime waterflow dynamics. Chapter 4 concludes the thesis by summarising the research and its main contributions to the disciplines of hydrometeorology and land-atmosphere interactions.

Chapter 2

Methods and Materials

2.1 RegCM4 description and simulation design

The ICTP–RegCM4 (Giorgi et al., 2012) is the latest generation of the (area-limited) regional climate model. The first significant enhancement to RegCM3 (Pal et al., 2007) resulted in code migration/re-writing from legacy Fortran77 to modern Fortran90/2003 code, with implementation of message passing interface (MPI) to facilitate two-dimensional parallel processing. This latest code development increased its machine scalability, as well as its computational efficiency (Giorgi et al., 2012). The dynamic core of the model was also revised to incorporate assumptions of non-hydrostatic pressure and feedback interactions with newly enhanced modules of physicochemical processes of the atmosphere.

The model's governing equations are based on equations of momentum, thermodynamics, and state (Anthes et al., 1987). The fundamental, diagnostic model variables are the horizontal (u; in the west-to-east direction) and lateral wind velocity fields (v; south-to-north direction), and scalar fields, such as air temperature (T), specific humidity (q), and atmospheric pressure (p). RegCM4 uses a B-staggering horizontal mesh, where the wind velocity components (i.e., u, v) are defined at the cell vertices, whereas scalar quantities like T, q, and p, are defined at the cell centre (Figure 1). RegCM4 has a terrain-following vertical coordinate system (σ) defined by eqn. (1) and illustrated in Figure 2. All vertical components are defined with respect to σ, i.e.,

$$\sigma = \frac{p - p_t}{p_s - p_t} \tag{1}$$

where p is the pressure in hPa at any vertical level in the atmosphere, p_s surface pressure, and p_t specified atmospheric pressure at the model's top level. Here, σ ranges between 1.0 at the earth's surface and 0.0 at the prescribed upper level of the atmosphere.

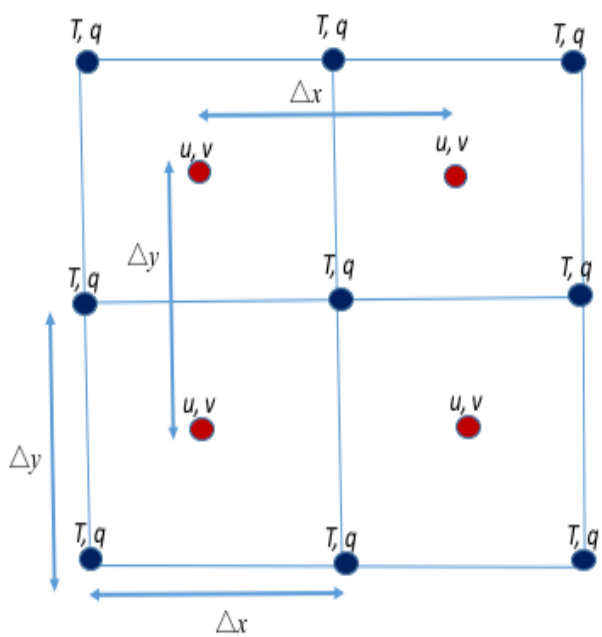

Figure 1. B-staggered horizontal grid, with Δ*x* and Δ*y* representing the horizontal resolutions in both the *x* and *y* direction.

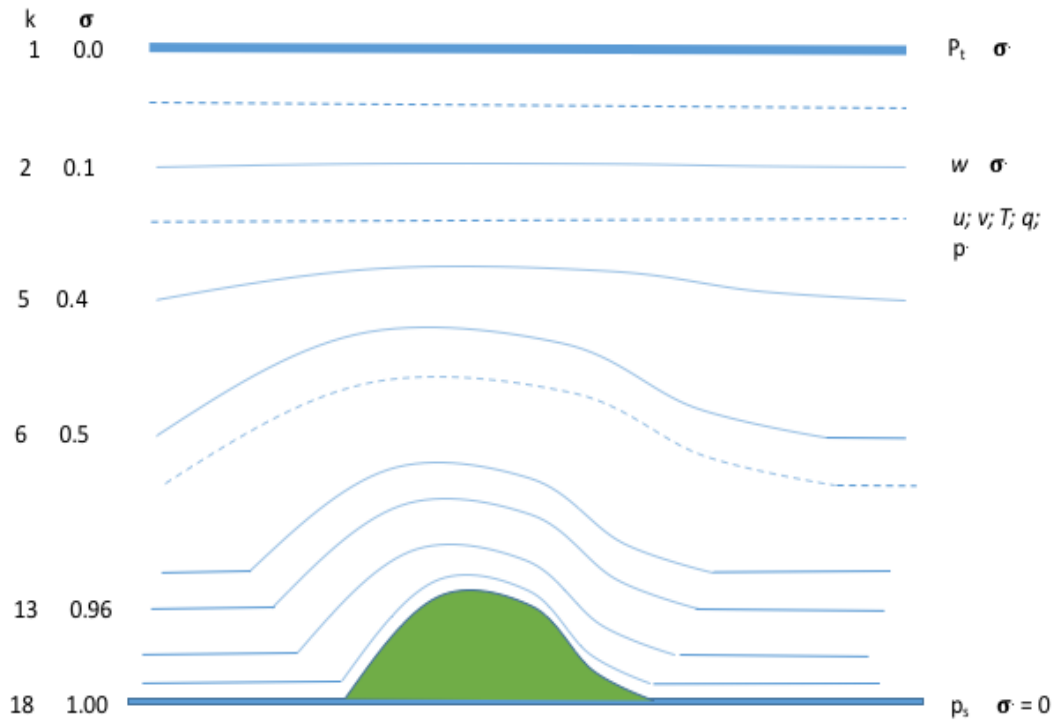

Figure 2. Schematic of the terrain-following coordinate system. This schematic shows 11 vertical layers as a function of topography. The dashed lines represent ½-σ levels, whereas the solid lines represent full-σ levels.

The current formulation of RegCM4 addresses both hydrostatic and non-hydrostatic atmospheric conditions (Grell et al., 1994), land-atmosphere interactions by means of a biosphere-atmosphere transfer scheme (BATS; Dickinson et al., 1993), shortwave and longwave energy exchange, planetary boundary layer (PBL) forcing, and various options for the treatment of convection and cloud micro-physics. The model user must carefully select the combination of model options to best replicate seasonal atmospheric conditions and stream and river flow dynamics in Maritime Canada.

The non-hydrostatic dynamic core accounts for an explicit treatment of convection at high spatial resolution, defined here at 5 km. Hydrometeorological processes relevant to the study area, such as sub-soil and surface-soil temperatures, surface runoff, and snowmelt are modelled through the BATS module (Dickinson, 1988). The nonlocal, PBL scheme of Holtslag et al. (i.e., Holtslag et al., 1990) provides the numerical treatment of vertical transport of moisture and heat from the surface upward to the free atmosphere (beyond the top level of the simulated atmosphere; Figure 2). The subgrid explicit moisture scheme in the model addresses the non-convective formation of clouds and precipitation at large spatial scales (Pal et al., 2000). The scheme relates the average grid-cell relative humidity to cloud fraction and cloud liquid water content (Sundqvist et al., 1989).

The model's initial and boundary conditions are based on the European Centre for Medium-Range Weather Forecast (ECMWF), ERA-Interim data (Uppala et al., 2008). The data is provided at 0.25° resolution globally, at 6-hour intervals, for all dynamic state variables, u, v, T, q, and p_s. ERA-Interim [global climate model (GCM)-generated timeseries] prescribes the sea surface temperature with a resolution of 1.5°, also at 6-hour intervals. The data is interpolated to 5-km grid resolution for the designated RegCM4-simulations from 2007–2019.

RegCM4 considers a mesh of 200 × 200 grid cells, with 18 vertical atmospheric layers, extending from the surface to 50-hPa (Figure 1, 2). The computational domain is chosen here to have the upper Wolastoq basin located at its centre (Figure 3).

RegCM4 uses the USGS global landcover characterization (GLCC) data to define its surface boundary condition. It is based on 1-km AVHRR (Advanced Very High-Resolution Radiometer) data. The data are collected from April 1992 to March 1993. These

data have been interpolated to the model domain resolution, i.e., 5-km resolution. The data are classified into 21 categories, namely, crop, short grass, evergreen trees, deciduous trees, and so on, each assigned an integer from 0 to 21 (Figure 4).

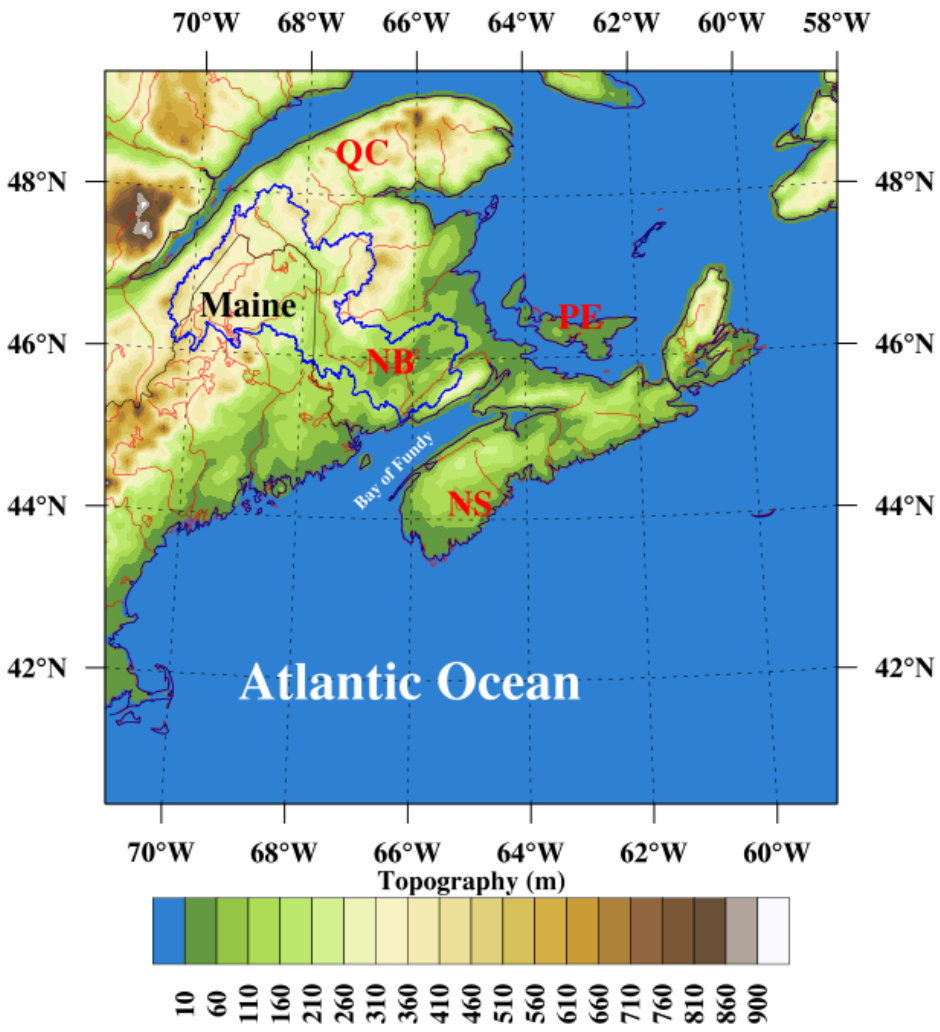

Figure 3. Computational domain. The blue polygon outlines the Wolastoq basin. The computational domain includes the three Maritime provinces [i.e., New Brunswick (NB), Nova Scotia (NS), and Prince Edward Island (PE)], the southeastern-most part of Quebec (QC), and northeastern Maine (ME), USA. The variation in background colours represent changes in elevation (legend).

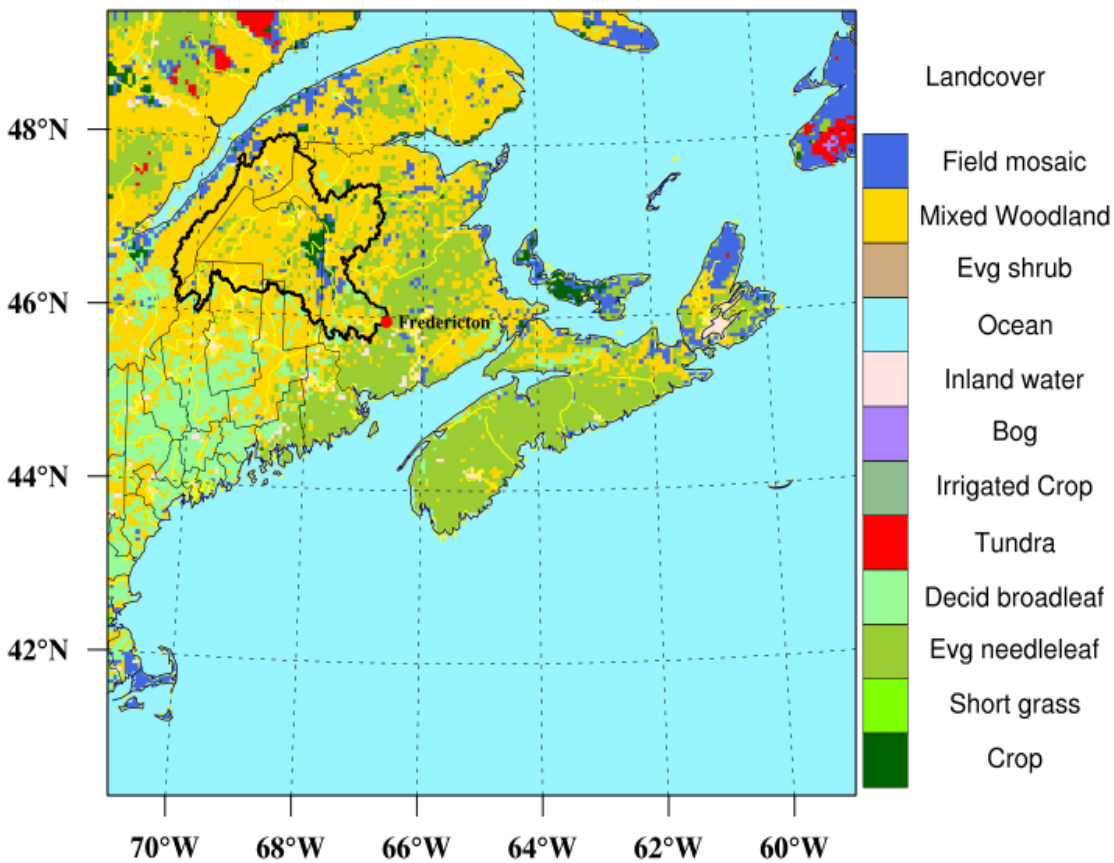

Figure 4. Landcover categories (legend). The black polygon outlines the upper Wolastoq basin; the red circle represents the city of Fredericton and outlet of the upper Wolastoq basin.

2.2 Snow parameterisation

Snowmelt rate (S_m) in BATS is derived from the energy-balance equation, i.e.,

$$L_f \; S_m = S_g + F_{IR}^{\downarrow} - F_{IR}^{\uparrow} - F_s - L_v F_q - h_s \qquad (2)$$

where L_f is the latent heat of fusion, S_g solar radiation flux density absorbed by the snowpack, $F_{IR}^{\downarrow}$ and $F_{IR}^{\uparrow}$ downwelling and upwelling thermal, infrared radiation, and F_s, $L_v F_q$, and h_s sensible, latent, and ground heat fluxes (all in W m^{-2}), respectively. The snowmelt rate is calculated following the solution of ground temperature determined with a heat diffusion equation for porous soils (Dickinson et al. 1993).

Other important factors related to snowmelt is the snow cover extent, snow age, and snow depth. The fraction of the computational grid covered by snow f_{snow} is parameterised following a monotonic increasing function of mean snow depth $f_{sn}(m)$ and it ranges from 0.0–1.0, i.e.,

$$f_{snow} = \frac{f_{sn}}{1 + f_{sn}} \tag{3}$$

where f_{sn} is the ratio of snow water equivalent (S_{cv}) to the snow's density (ρ_{sw}), relative to its liquid water density,

$$f_{sn} = 0.1 \frac{S_{cv}}{\rho_{sw}\, Z_{\circ}} \tag{4}$$

where $Z_{\circ}$ is a pre-assigned aerodynamic roughness length given in metre, it depends on land cover category, it ranges from 0.0024 (for ocean and lakes) to 2 m (evergreen broadleaf trees). The snow water equivalent in BATS is parameterised by the following equation,

$$\frac{\partial S_{cv}}{\partial t} = P_{sw} - \left(F_q + S_m\right), \tag{5}$$

where P_{sw} and F_q are the snowfall rate and snow sublimation-evaporation rate, respectively. Finally, from the water balance equation, cumulative surface runoff (R_s) over winter and spring is defined as

$$\sum R_s = \sum [\left(P_{sw} + (S_m - F_q\right)] \,. \tag{6}$$

2.3 Landcover change sensitivity experiment

The landcover of the upper Wolastoq basin is digitally altered from forests/woodland to crop cover, reflecting the accumulation of repeated annual forest-cover removal (due to legacy effects) and exposure of residual short-statured vegetation and ground surface over the 12-year simulation period. This landcover substitution forms the landcover change experiment (LU) to be addressed later, whereas no annual substitution constitutes the control (CTL).

The LU-experiment is guided by Global Forest Watch (GFW) shapefiles, expressing annual forest-cover removal for each subbasin based on an analysis of Landsat images (Linke et al., 2017). To digitally alter the landcover, each GFW polygon is mapped to the model's domain using NCAR Graphics Language (NCL) to extract all pixels within each polygon. Then with FORTRAN-script, all pixels within individual polygons are re-labelled

as short grass and cropland cover (via their assigned category number). Table 1 specifies GFW-based landcover data for subbasins in the upper Wolastoq basin > 1,000 km^2 (Figure 5a). For instance, in 2008, 0.7% of subbasin 01AF002 was cleared, increasing the total forest loss during that year to 4.6%. In 2018, 247.27 km^2 of forest was removed, accounting for 1.1% of the subbasin area. Altogether, 12.4% of the subbasin was cleared from 2001–2018 (Table 1 and Figure 5b). Figure 6 gives the digital landcover surfaces for the CTL- and LU-experiments for the 2001–2008 and 2001–2018 simulation periods, respectively.

Table 1. Upper Wolastoq basin cumulative forest-removal; third and fourth columns represent the total within subbasin forest-area harvested (in km^2) and current year and cumulative % removal (in brackets) from 2001 to 2008 (column three) and from 2001 to 2018 (column four), respectively.

Subbasin ID	**Subbasin Area** (km^2)	**2008**	**2018**
01AF002	21,724	144.50 (0.67,4.58)	247.27 (1.14,12.39)
01AD004	15,386	107.75 (0.70,4.42)	164.16 (1.07,11.59)
01AD002	14,607	104.81 (0.72,4.47)	159.2 (1.09,11.66)
01AG003	6,097	2.84 (0.05,0.27)	4.78 (0.08,0.95)
01AE001	2,257	13.08 (0.58,4.71)	34.94 (1.55,13.88)
01AH002	2,231	19.47 (0.87,9.09)	35.68 (1.60,25.08)
01AJ003	1,207	3.47 (0.29,3.53)	5.04 (0.42,9.41)
01AF010	1,030	16.74 (1.63,9.62)	16.81 (1.63,27.70)

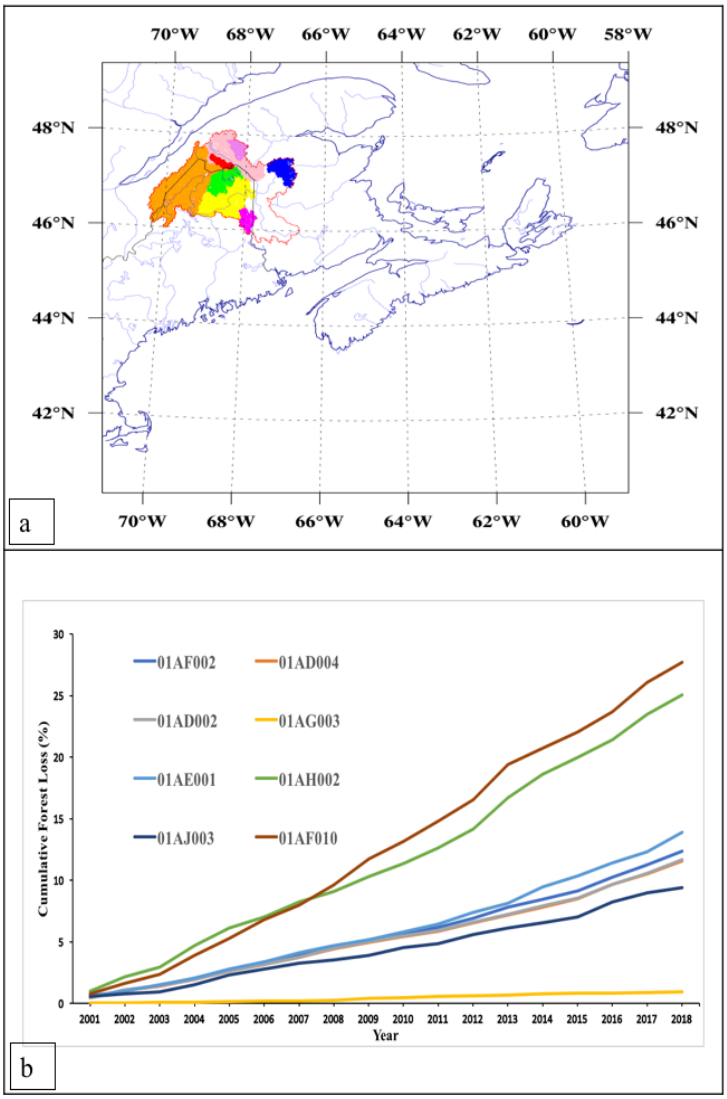

Figure 5. (a) Upper Wolastoq basin and its eight large subbasins, including 01AF002 (polygon coloured in pink), 01AD004 (red), 01AD002 (orange), 01AG003 (yellow), 01AE001 (green), 01AH002 (blue), 01AJ003 (magenta), and 01AF010 (violet). Note that subbasins 01AD004 and 01AD002 make up part of subbasin 01AF002. Panel (b) gives the cumulative annual forest-cover loss in % of subbasin areas from 2001–2018.

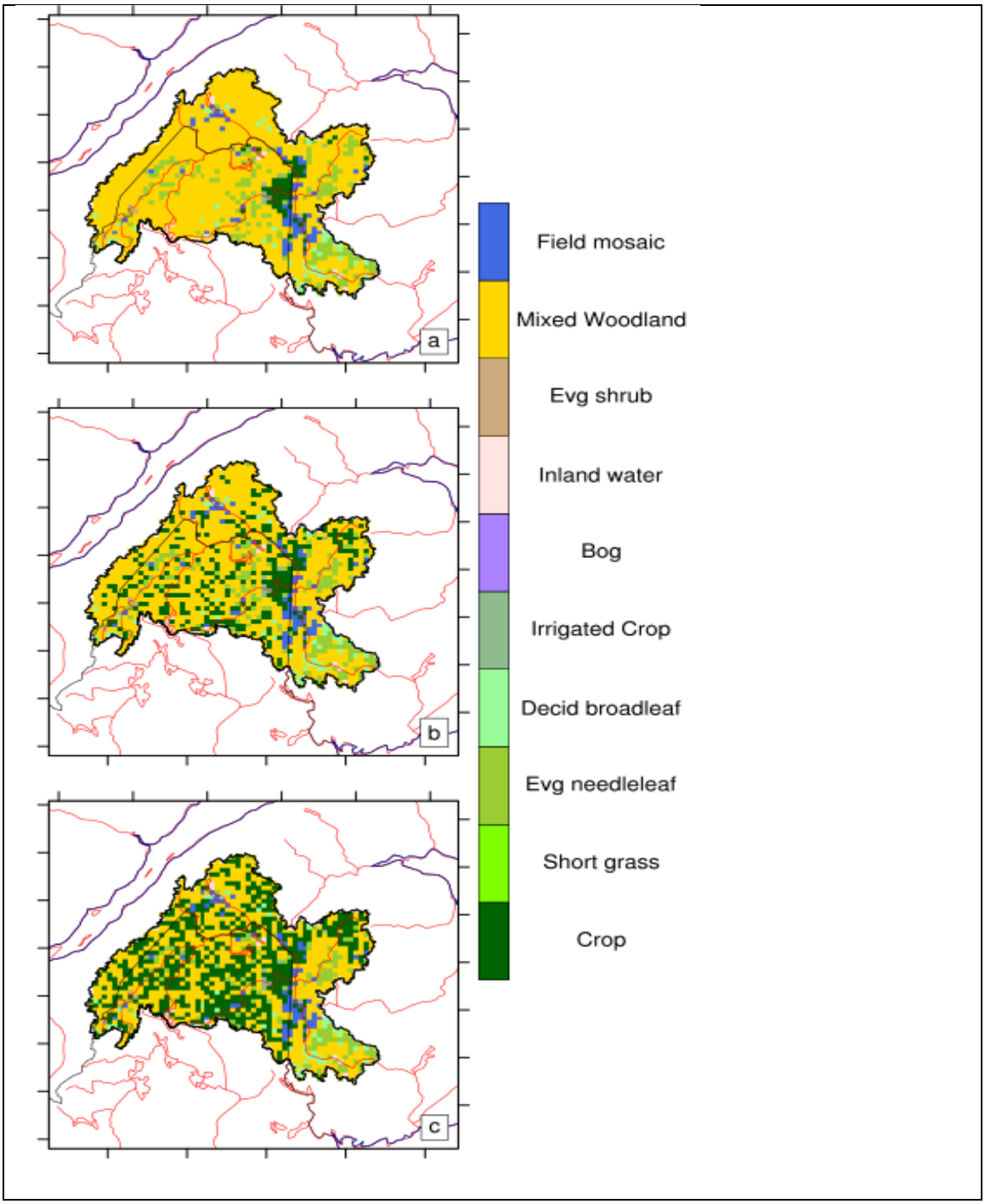

Figure 6. Landcover change in the upper Wolastoq basin, whereby mixed woodlands and evergreen needleleaf (green and gold) are replaced by short grass (light green) and crop (dark green). Panel (a) gives the landcover for the control run (CTL), and panels (b) and (c) cumulative annual forest-cover loss from 2001–2008 and 2001–2018 (LU), respectively.

2.4 Datasets and statistical analysis

Modelled mean, maximum, and minimum air temperatures and annual total precipitation are compared against measured data at 11 climate stations managed by Environment and Climate Change Canada (https://climate.weather.gc.ca). The 11 stations were selected according to (i) their position in the computational domain; (ii) availability of uninterrupted daily weather data over the simulation period from 2007–2019; and (iii) availability of climate normals for 1980–2010.

Table 2 lists the climate stations used in assessing model performance. These stations are representative of various climatic zones in the upper Wolastoq (column six of Table 2). For example, Causapscal (QC) represents conditions in the Notre Dame Mountains and Wolastoq's headwaters, and Fredericton CDA (NB), lowland-valley conditions at the basin outlet.

Fundamental characteristics of model performance is based on the root mean squared error (RMSE), model bias ($\bar{E}$), and correlation (R) between RegCM4-simulated and climate station-observed values. Taylor diagrams (Taylor, 2001), by virtue of their design, capture the essential elements of model performance in a single diagram. The data comparisons are partitioned according to their season of occurrence, i.e., fall (spanning the months of September to November, or SON), winter (December to February, DJF), spring (March to May, MAM), and summer (June to August, JJA).

Here, we denote the time averages of modelled and observed values over N days as $\bar{m}$ and $\bar{o}$, respectively; the mean model bias, or $\bar{E}$, is determined as

$$\bar{E} = \bar{m} - \bar{o}. \tag{7}$$

The correlation (R) between modelled and observed values is calculated using Pearson's correlation coefficient, or

$$R = \frac{\frac{1}{N}\sum_i^N (m_i - \bar{m})(o_i - \bar{o})}{\sigma_m \sigma_o}, \tag{8}$$

where σ_m and σ_o are the standard deviations for both projected and observed values. The RMSE is defined as:

$$E = \left[\frac{1}{N}\sum_i^N (m_i - o_i)^2\right]^{\frac{1}{2}}. \tag{9}$$

A new performance metric named the centred-pattern-RMSE is defined as

$$\tilde{E} = \left[\frac{1}{N}\sum_i^N [(m_i - \bar{m}) - (o_i - \bar{o})]^2\right]^{\frac{1}{2}}. \tag{10}$$

It is straightforward to demonstrate that

$$E^2 = \tilde{E}^2 + \bar{E}^2. \tag{11}$$

The Taylor diagram is founded on the cosine law, or

$$c^2 = a^2 + b^2 - 2ab\cos\theta, \tag{12}$$

where a, b, and c are the side lengths of a triangle and θ is the angle between sides a and b. The Taylor diagram relates the correlation R, $\tilde{E}$, σ_m, and σ_o in the same fashion, whereby

$$\tilde{E}^2 = \sigma_m^2 + \sigma_o^2 - 2\sigma_m\sigma_o R. \tag{13}$$

A geometric interpretation of eqn. (13) is a triangle with σ_o as its base, σ_m as its second side that is rotated counterclockwise with an angle $\cos^{-1} R$, and $\tilde{E}$ as the length of its third side (Taylor, 2001). It is better to construct the Taylor diagram using normalised values, by dividing eqn. (13) by $\sigma_o{}^2$. This is useful in plotting different parameters with different units on the same diagram. In a Taylor diagram (i) the radial distance from the origin is proportional to the normalised standard deviation, (ii) the centred-pattern-RMSE is the radial distance from the reference point (i.e., REF) on the diagram, and (iii) the correlation between model-projections and observations is given by the azimuthal position of the station marker. The REF point on the Taylor diagram represents perfect model performance with 100% correlation, equal standard deviation, and zero error (Chapter 3).

Table 2. Representative climate stations within Maritime Canada.

#	Station ID	Station Name	Province	Latitude	Longitude	Climate Type
1	7051200	Causapscal	QC	48.37	-67.23	Mountain
2	8101303	Edmundston	NB	47.42	-68.32	Mountain
3	8105600	Woodstock	NB	46.17	-67.55	Valley
4	8102536	Mactaquac Prov Park	NB	45.95	-66.90	Valley
5	8101605	Fredericton CDA	NB	45.92	-66.61	Valley
6	8101794	Gagetown AWOS	NB	45.84	-66.45	Valley
7	8103100	St. Stephen	NB	45.21	-67.25	Valley
8	8101925	Grand Manan SAR	NB	44.71	-66.80	Maritime
9	8200604	Brier Island	NS	44.29	-66.35	Maritime
10	8200255	Baccaro Point	NS	43.45	-65.47	Maritime
11	8300418	East Point	PEI	46.46	-61.99	Maritime

Chapter 3

Results and Discussion

3.1 New Brunswick climatology and model validation

Modelled and observed air temperature and precipitation and their statistical summaries were evaluated for the St. Pamphile station next to Mount Notre Dame, QC (Figure 7). Comparison wise, this station provided reasonable accuracy among the 90 climate stations employed in the study. Temperature analysis (Figure 7a) showed that the model captured the annual mean, minimum, and maximum temperature cycles, and associated temperature ranges reasonably well across all seasons. Minimum and mean temperatures were closest to their corresponding values associated with the normal period (1980–2010). This was not the case for maximum temperature. The model, on average, overestimated the mean temperature by 4°C in winter and 2°C in summer, respectively.

Modelled minimum temperatures were appreciably lower than their equivalents during the normal period, i.e., the model was cooler than actual conditions, and associated differences decreased from 8°C during the cold to 4°C during the warm seasons. The modelled maximum temperatures were mostly greater than those for the normal period. The difference was most significant during the cold season (up to 14°C), which dropped to 6°C during the warm seasons. In summary, RegCM4-generated calculations of air temperature were generally cooler than those observed at night and warmer at mid-afternoon across all seasons. This discrepancy may be attributed to the choice of parameterisation used in the numerical treatment of the PBL.

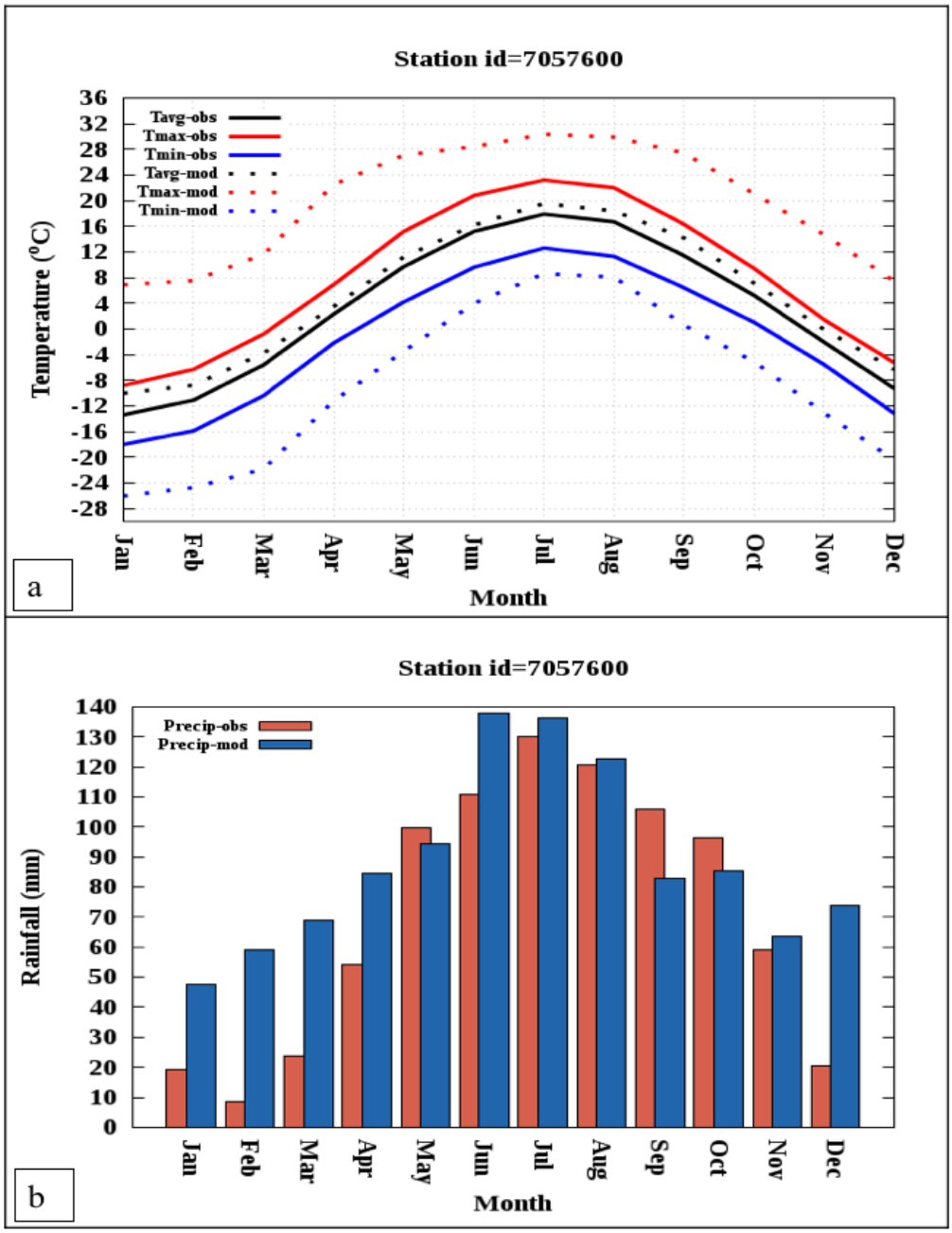

Figure 7. Observed and modelled (a) monthly mean, maximum, and minimum air temperatures and (b) total precipitation at St. Pamphile, QC (Station ID=7057600; see legend). Observed and modelled data are representative of the normal period from 1980–2010 and the simulation period from 2007–2019, respectively.

Figure 7b highlights the degree to which the modelled monthly precipitation cycle reproduces the actual cycle, producing a minimum during winter (i.e., DJF) with 10–20 mm of precipitation and a maximum during summer (JJA) with 110–130 mm. In general, the model overestimated precipitation, particularly in summer. There were instances, the model produced drier conditions than observed during the normal period. This is especially the case for the months of September and October (Figure 7b). In a subsequent precipitation analysis based on Fredericton station data, the average trends were very similar to those observed for St. Pamphile (Figure 7). Again, the model was generally cooler at night and warmer at mid-afternoon, with modelled mean air temperatures deviating the least from observed 30-year means (Figure 8a).

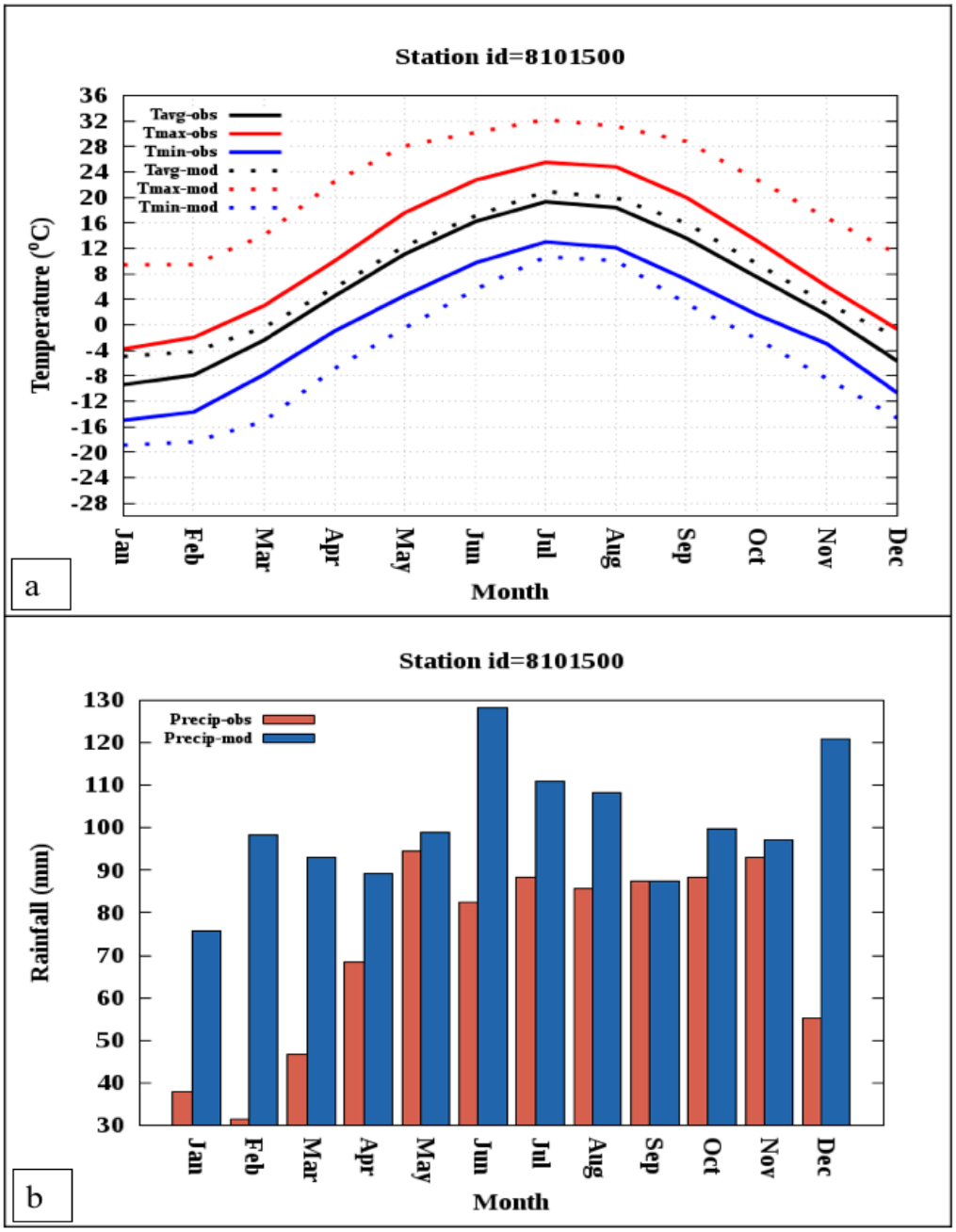

Figure 8. Observed and modelled (a) monthly mean, maximum, and minimum air temperatures and (b) total precipitation at Fredericton, NB (Station ID=8101500; see legend). Observed and modelled data are representative of the normal period from 1980–2010 and the simulation period from 2007–2019, respectively.

For Fredericton, the rainy season tended to span the May–November period of each year (Figure 8b). The model exhibited some altered behaviour relative to trends observed in the climate data from St. Pamphile, QC. Overall, the model overestimated precipitation for most of the year with excessive precipitation occurring in winter (i.e., DJF). The model was able to accurately simulate late-spring and early-fall precipitation levels (Figure 8b).

Comparisons of autumn and spring modelled, and 30-year mean daily temperature summaries exhibited the greatest level of correlation, lowest RMSE, and minimum relative variability (i.e., SON and MAM, Figure 9a). Inland stations No. 1–7 were shown to provide the best overall agreement between modelled and 30-year data summaries. In contrast, coastal stations (i.e., stations No. 8–11) provided the least favourable agreement. This discrepancy may have occurred because of the computational domain's relatively coarse resolution (i.e., at 5 km). Land-sea interfaces in the model were poorly differentiated, introducing numerical artefacts at these coastal stations. For example, Grand Manan and Brier Island stations (climate stations No. 8 and 9, respectively) were seen by the model as occurring over ocean water, causing discrepancy between observed and simulated datasets, particularly in summer. This is reflected in low correlation and high centred-pattern-RMSE. In general, a significant portion of climate stations provided coefficients of correlation > 90% and normalised RMSE < 50% across all seasons (Figure 9a).

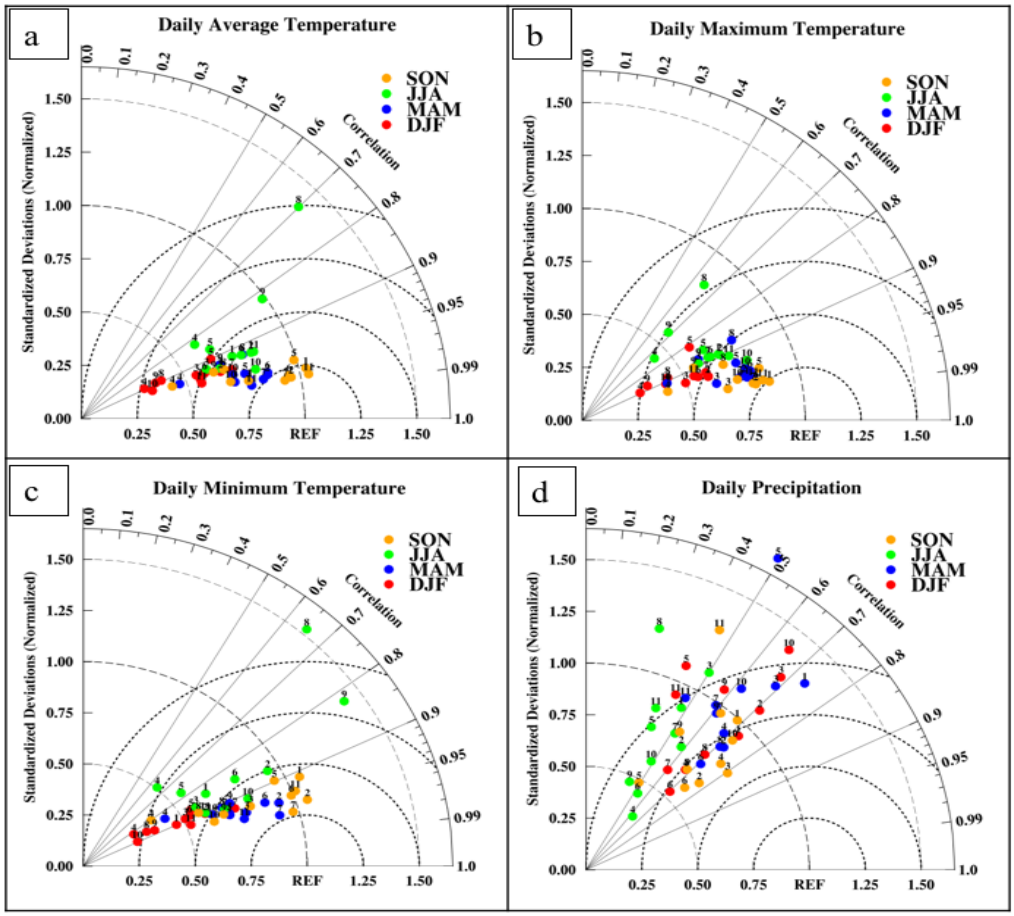

Figure 9. Taylor diagrams of daily (a) mean, (b) maximum, (c) minimum air temperatures, and (d) total precipitation for 11 stations in the upper Wolastoq basin. The data are representative of the 2007–2019 simulation period. Colours coincide with season (legend) and the stations are ordered from north to south.

Daily maximum and minimum air temperatures are determined by the vertical diffusion of heat and moisture fluxes in the PBL (Stull, 1988). Comparison of actual and simulated maximum and minimum temperature summaries showed that corresponding 30-year mean daily maximum temperatures provided the greatest correlation (at > 95%) and the lowest centred-pattern-RMSE (< 35%). Modelled and 30-year mean daily minimum

temperatures provided comparable variability across the set of climate stations (Figure 9b, c).

Comparison of the 30-year mean and modelled daily total precipitation exhibited much greater scatter (Taylor diagram, Figure 9d). Correlation varied between 60 and 80% in autumn, winter, and spring, with the lowest correlation occurring in summer. Data variability was highly non-uniform, yielding high RMSE-values, mostly > 100% (Figure 9d). We attribute these discrepancies to the following model limitations: (i) although simulations are performed here at a 5-km resolution, generally detailed relative to available global and regional climate simulations, RegCM4 fail to capture local climatologies associated with maritime and mountain settings; and (ii) current model parameterization of PBL and large-scale precipitation are based on untested, simplified schemes that do not necessarily apply to high-resolution climate modelling.

3.2 Spring flooding of 2008

Sequencing of hydrometeorological processes from January–April 2008 gave rise to the occurrence of the 2008 flooding event. In January, the upper Wolastoq basin experienced an enormous amount of snow on the ground. This amount continued to increase through February–April (snow ablation during this time was low), giving abnormal amounts by the end of the snow accumulation season (e.g., ~1.6 m at the St. Camille weather station, QC, in the headwaters of the upper Wolastoq). Given the deep snowpack in the headwaters, melting snow during the last week of April–May caused acute surface runoff and high discharge rates (Figure 10).

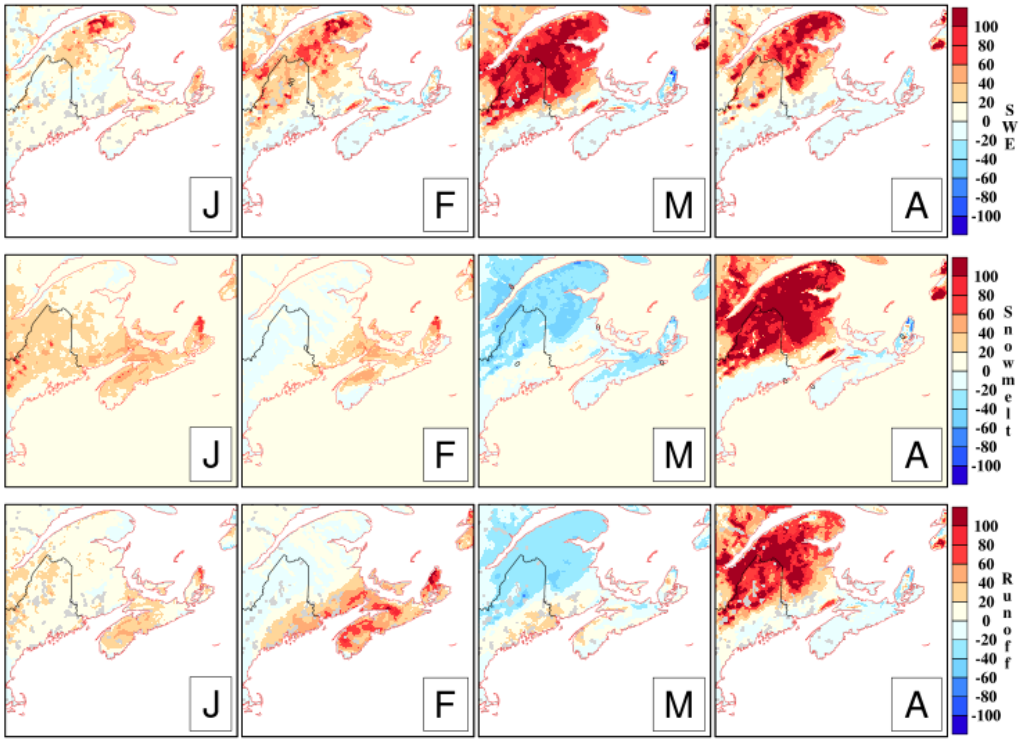

Figure 10. Modelled monthly anomalies of on-the-ground snow water equivalent (SWE), snowmelt, and surface runoff for January (J), February (F), March (M), and April (A) of 2008. Warm colours (shades of red) represent positive monthly anomalies above normal (calculated from modelled data from 2007–2019), whereas cool colours (shades of blue, see legend) represent negative anomalies below normal.

The following analyses show timeseries of RegCM4-modelled anomalies for total precipitation, on-the-ground SWE, snowmelt, snow sublimation/evaporation of melted snow, and surface runoff for 12 consecutive years of simulation, averaged over the upper Wolastoq basin (Figure 11–15). The anomalies point to the timing in hydroclimatic variables relative to that of flooding in the upper Wolastoq.

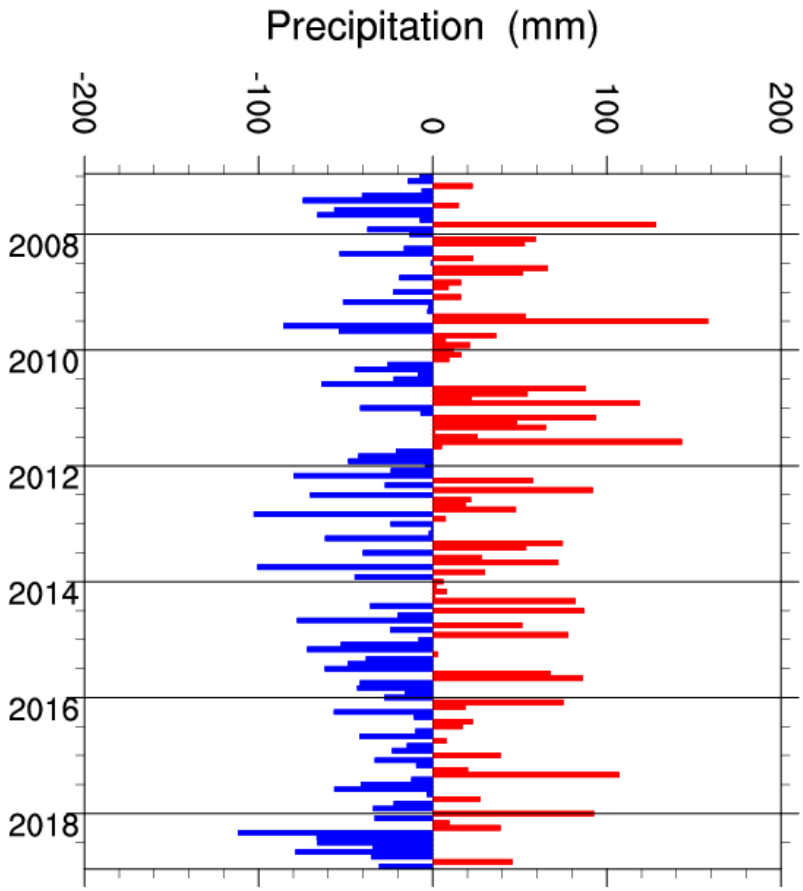

Figure 11. Modelled monthly anomalies of total precipitation, where the red bars denote deviations above normal and blue bars, deviations below normal. The central line or normal gives the mean for the simulation period of 2007–2018.

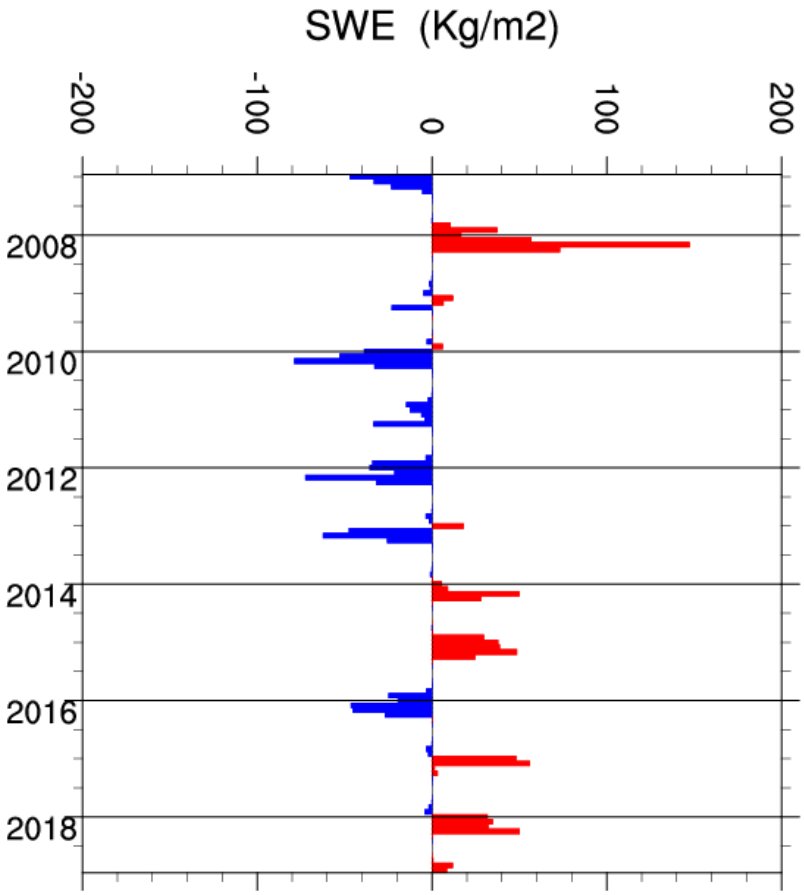

Figure 12. Modelled monthly anomalies of on-the-ground snow water equivalent, where the red bars denote deviations above normal and blue bars, deviations below normal. The central line or normal gives the mean for the simulation period of 2007–2018.

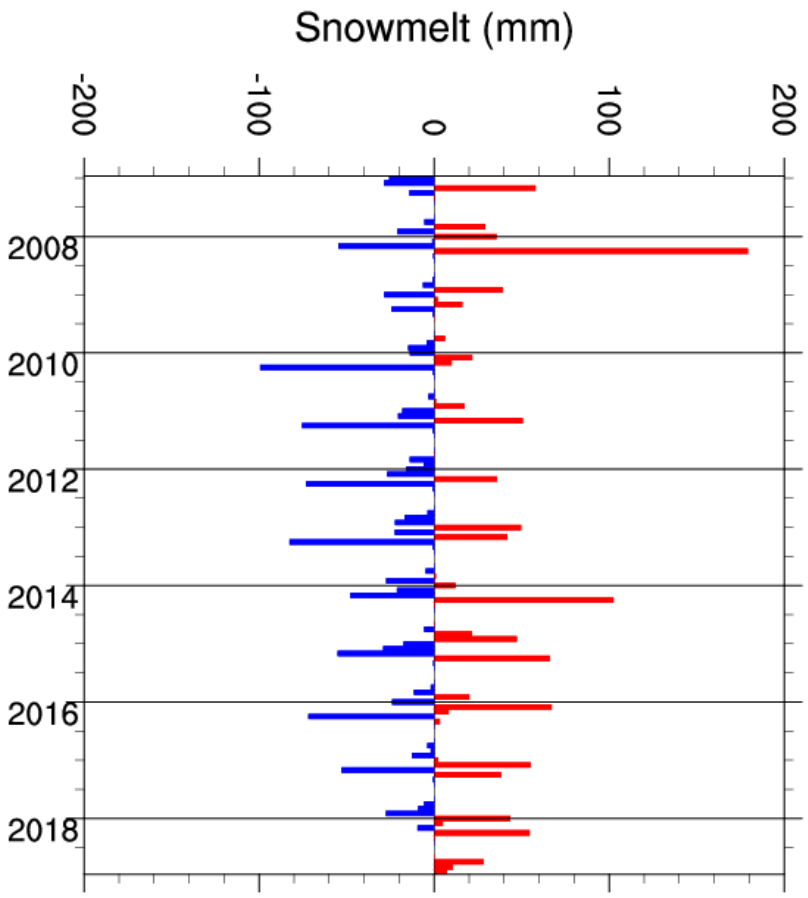

Figure 13. Modelled monthly anomalies of snowmelt, where the red bars denote deviations above normal and blue bars, deviations below normal. The central line or normal gives the mean for the simulation period of 2007–2018.

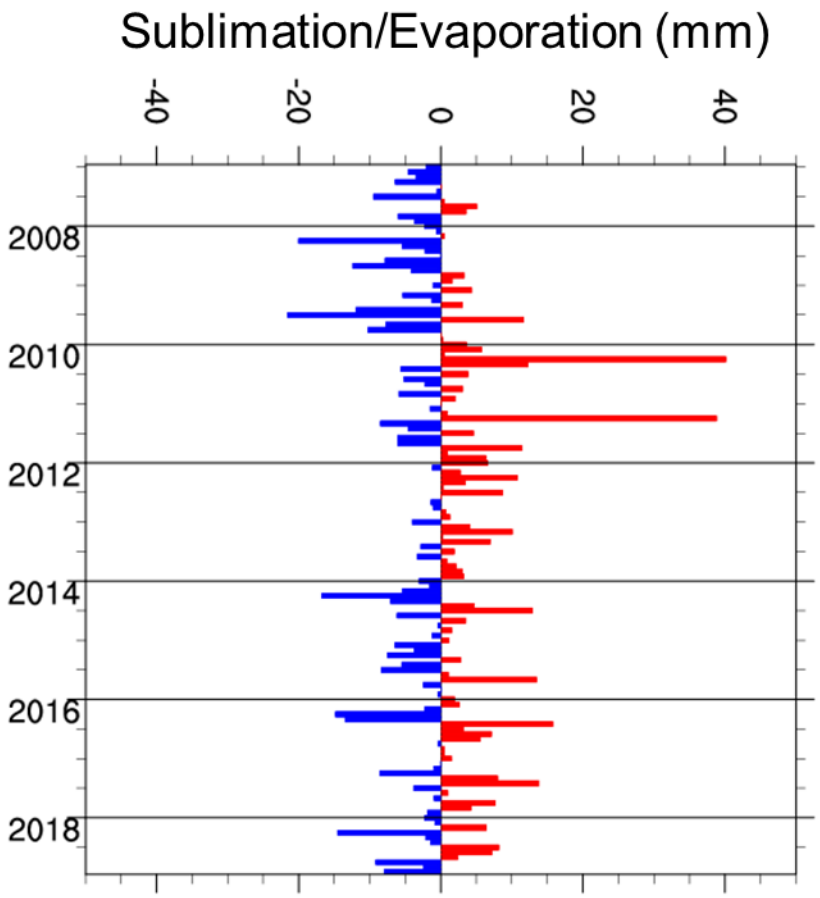

Figure 14. Modelled monthly anomalies of sublimation/evaporation, where the red bars denote deviations above normal and blue bars, deviations below normal. The central line or normal gives the mean for the simulation period of 2007–2018.

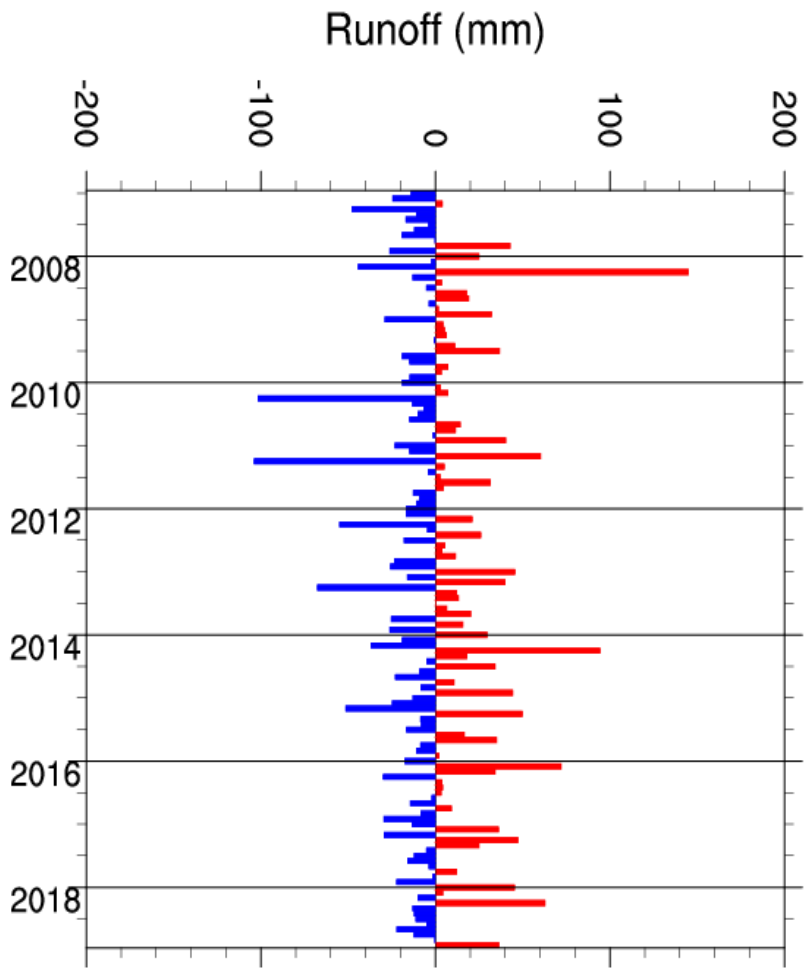

Figure 15. Modelled monthly anomalies of surface runoff, where the red bars denote deviations above normal and blue bars, deviations below normal. The central line or normal gives the mean for the simulation period of 2007–2018.

Simulated monthly anomalies of total precipitation varied between -120 to 160 mm (Figure 11). November 2007, February, and March 2008 showed an intense snowfall, approximately 140, 60, and 50 mm above normal, respectively. Simulated monthly anomalies of on-the-ground snow water equivalent (SWE) for 2007–2019 varied between -100 to 100 kg m^{-2} (Figure 12). These anomalous snowfall events strongly enhanced the development of the within-basin snowpack during that period. Accordingly, simulated

snowmelt during the melt season of each year followed comparable trends (Figure 13), varying between -100 to 180 mm. March 2008 illustrated a sharp decline in snowmelt in early spring coinciding with the increased snowpack. In April 2008, ample snowmelt that resulted (+180 mm above the mean) contributed to substantial surface runoff. Total simulated monthly anomalies of sublimation and evaporation varied between -20 to 40 mm. This shows that sublimation/evaporation played a minor role in reducing snow cover from November 2007–April 2008 (Figure 14).

Simulated monthly anomalies of surface runoff varied between -100 to 100 mm (Figure 15). In March 2008, surface runoff was less than the 2007–2019 mean by 45 mm, followed by a significant jump to +140 mm above the mean in April 2008. Significant surface runoff at that time could be largely attributed to the unprecedented snowpack buildup in the preceding four months. Other factors of importance that contributed to the 2008 spring flooding were related to the synoptic-scale forcing associated with airmasses, either from the northwest in winter or the southwest in spring. Freezing degree-days (FDD, i.e., $\sum T_{avg} < 0^{o}C$ over the November–March period), cumulative snow degree-days (SDD, i.e., $\sum T_{avg} > 0^{o}C$ over the March–May period), and mean wind speed determined the airmass characteristics that influenced the Wolastoq at that time. Temperature indices, FDD and SDD, can be viewed as proxies of snowpack accumulation and snowmelt, respectively. Table 3 gives the FDD and SDD derived from simulated near-surface air temperatures. Both snow accumulation and snowmelt seasons of 2008 were characterized by large FDD and SDD of about -959 and 450 degree-day units. Mean SDD was about 499 degree-day units, which was greater than the 75th percentile calculated from long-term observational data (Yu and Bourque, 2022).

Table 2. Freezing and snow degree-days, i.e., FDD and SDD (degree-day units), respectively; FDD is calculated for the November–April snow accumulation period, whereas SDD is calculated for the March–May snowmelt period of each year from 2007–2019.

	2008	**2009**	**2010**	**2011**	**2012**	**2013**	**2014**	**2015**	**2016**	**2017**	**2018**
FDD (NDJFMA)	-959	-944	-584	-796	-630	-767	-1115	-1098	-637	-806	-868
SDD (MAM)	450	483	597	523	588	520	457	496	462	510	450

The springtime flood of 2018 came as the second most significant flooding event, with a monthly anomaly of surface runoff of 70 mm above the 2007–2019 mean (Figure 11). RegCM4 was able to capture the excessive snowpack buildup in the winter and early spring of that year (Figure 12). This resulted in significant spring snowmelt of about 60 mm above the 2007–2019 mean (Figure 13).

3.3 Landcover change impact

Shifts in landcover produce changes in soil properties, snow-cover buildup, and surface fluxes. Table 4 gives the landcover-parameter changes undertaken within BATS to represent conversions from forests, in the control experiment (CTL), to short-statured residual vegetation in the landcover change experiment (LU; Dickinson et al., 1993). With conversion from forests to short vegetation post-disturbance, the landcover roughness length parameter (Z_o) is reduced to reflect the fact that open areas tend to promote greater on-the-ground capture of snow and increased snow-cover fractions [i.e., eqn. (4)]. Moreover, tree removal leads to a reduction in leaf area index (LAI; Table 4) and a

subsequent reduction in snow interception and its eventual sublimation (Reyes-González et al., 2019; Varhola et al., 2010; Lundberg and Halldin, 2001).

Table 3. Landcover-related parameters and their assigned values for both the landcover control (CTL) and landcover change experiments (LU).

Variable	CTL	LU
Maximum fractional vegetation cover	0.8	0.85
Fractional vegetation cover at 269 K	0.6	0.25
Fraction of water extracted by upper layer roots	0.5	0.3
Roughness length	0.8	0.06
Depth of the rooting zone soil layer (m)	2.0	1.0
Maximum LAI	6	6
Minimum LAI	3.0	0.5
Vegetation albedo for wavelength < 0.7	0.06	0.1
Vegetation albedo for wavelength > 0.7	0.24	0.30

At a regional scale, the upper Wolastoq basin discharge (i.e., water yield) is shown to be largely controlled, in descending order of importance, by SDD, SWE, forest-cover loss, ambient partial water vapor pressure (an indicator of in-air water vapour content), incident locally-available solar radiation, wind speed, and precipitation (Yu and Bourque, 2022). The Upper Wolastoq basin is characterized by deep snow accumulation (Dickison, 1981), the combination of anomalous SDD and SWE produce severe flooding events, as shown for the 2008 and 2018 model simulations. Landcover sensitivity in model simulations adds justification for the impact of landcover loss on basin-wide discharge rates.

The change in SWE in late winter and early spring is the difference between the forest-cover removal model experiment (LU) and the control run (CTL; Figure 16a, b). Snow water equivalent (SWE) increases in areas where the forest has been removed, with the greatest cumulative forest-cover removal arising by 2018 (Figure 5b, 6). Within-basin rates of snowmelt also increase with increased annual forest-cover removal, as demonstrated by Figure 17. This is consistent with the findings of numerous empirical studies reported in Varhola et al. (2010), where snowmelt rates were shown to increase by about 70% in open areas compared to forests.

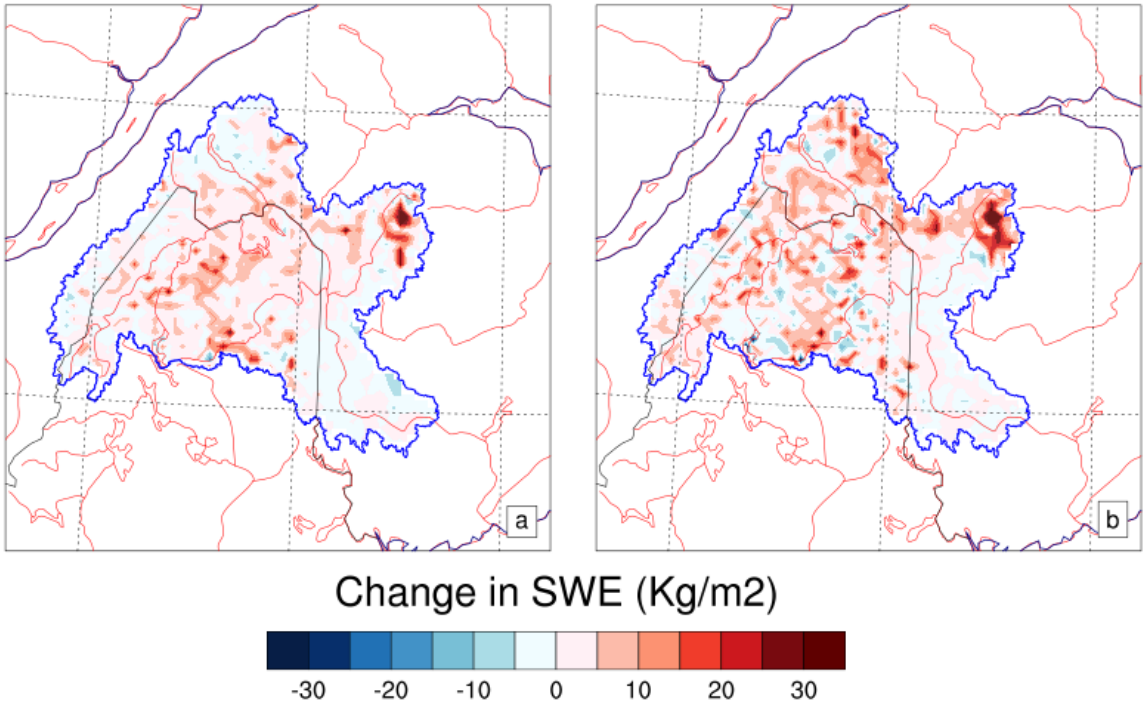

Figure 16. Changes in on-the-ground snow water equivalent (SWE) based on the difference between modelled snow ablation for the two landcover scenarios, LU and CTL, for the December–April period (i.e., DJFMA) of (a) 2008 and (b) 2018, respectively.

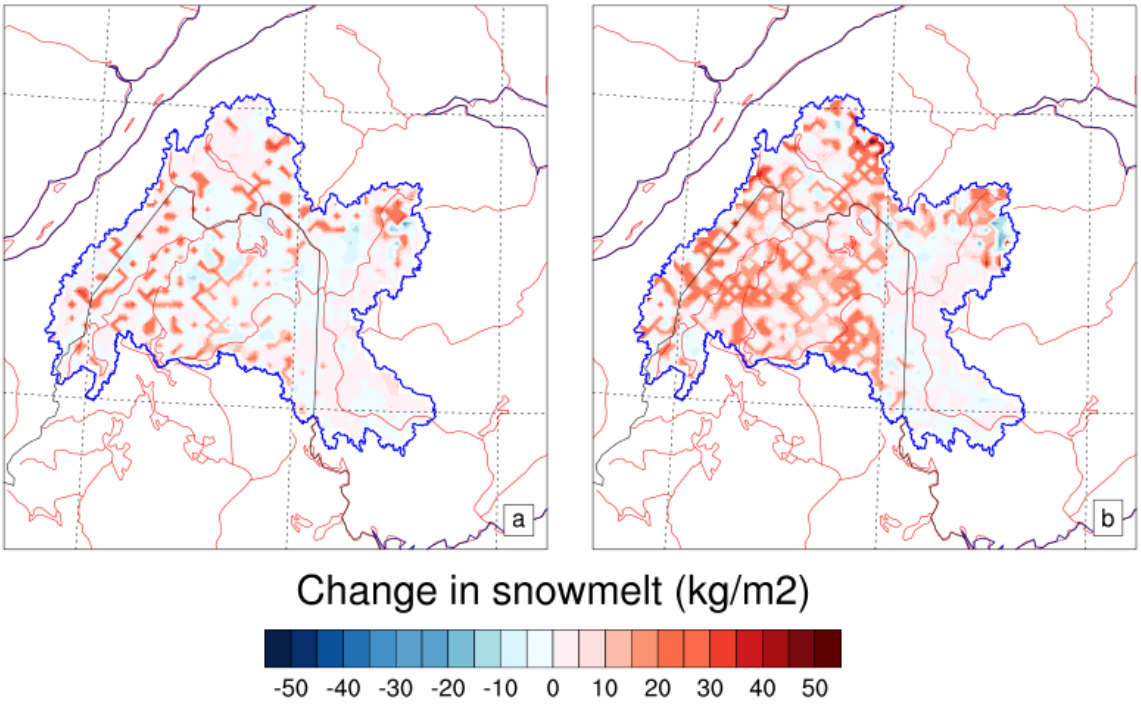

Figure 17. Changes in snowmelt based on the difference between modelled snowmelt for the two landcover scenarios, LU and CTL for the December–April period (i.e., DJFMA) of (a) 2008 and (b) 2018, respectively.

Modelled surface runoff is partitioned between the inputs of rainfall and snowmelt, and the output of snow sublimation, via eqn. (6). The large increase of snow on the ground due to forest-cover loss, outweighs the loss of snow through sublimation (e.g., Figure 11, 12, 14). The simulation shows that springtime surface runoff enhances in the upper Wolastoq basin from 2008–2018 (Figure 18a, b), due to increased cumulative forest-cover loss (Table 1 and Figure 5b, 6), despite peak on-the-ground snow cover was greatest in 2008 (Figure 12). The cumulative surface runoff increased by 27% in 2008 compared to 55% in 2018 at the end of the March–April period of each year (Figure 19). This upward trend is consistent with trends observed in an independent, empirical study of springtime

discharge rates and annual forest-cover removal in the upper Wolastoq basin (Yu and Bourque, 2022).

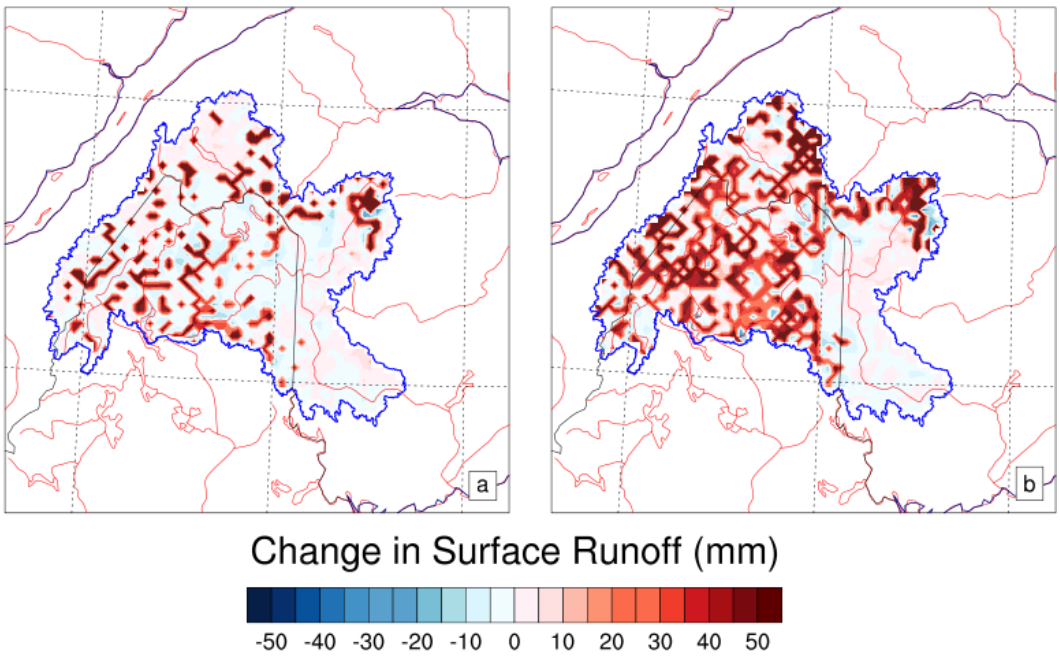

Figure 18. Changes in surface runoff based on the difference between modelled surface runoff for the two landcover scenarios, LU and CTL for the December–April period (i.e., DJFMA) of (a) 2008 and (b) 2018, respectively.

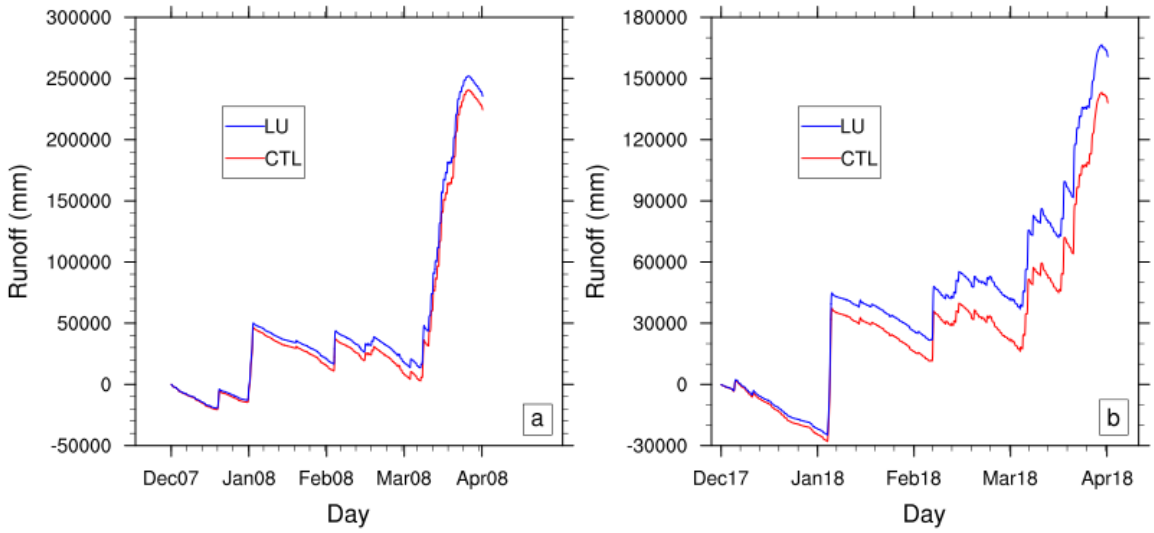

Figure 19. Cumulative surface runoff showing surface runoff summed over the upper Wolastoq basin for the December–April period (i.e., DJFMA) of (a) 2007–2008 and (b) 2017–2018, respectively. Red and blue lines represent the modelled control (CTL) and landcover change experiment (LU), respectively.

Chapter 4

Conclusions

The main objective of this thesis was to test whether repeated annual forest-cover removal in the upper Wolastoq basin caused basin discharge rates to increase, potentially escalating the risk of spring flooding further downstream. The regional climate model used here, i.e., RegCM4, successfully simulated air temperature and precipitation within Maritime Canada, as well as the major spring flooding events of 2008 and 2018. The landcover sensitivity experiment shows that progressive forest-cover removal in the last two decades had a direct role in increasing basin-wide snowmelt rates and surface runoff during the spring freshet of 2008 and 2018. It shows that discharge rates increased from 27 to 55% in 2008 and 2018, respectively, notwithstanding that peak snow cover was greatest in 2008.

Noteworthy are the limitations of this study. Model uncertainties imposed by the domain resolution and model simplifying assumptions have introduced some level of numerical bias in daily estimates of air temperature and precipitation from 2007–2019. These biases can be expected to impact the general description of the climate produced, but the trends observed in the impact of repeated annual forest-cover loss on basin discharge rates are largely consistent with those observed in a recent empirical study by Yu and Bourque (2022). Model improvement to account for more credible climate projections, especially for maritime and mountains locations, is beyond the available computational resources and the current model architecture.

References

Ahrens, C. D., P. L. Jackson, and C. E. J. Jackson, 2016: *Meteorology Today*. second can. Nelson Education,.

Anthes, R. A., E. Y. Hsie, and Y.-H. Kuo, 1987: *Description of the Penn State / NCAR mesoscale model version 4 (MM4), NCAR Tech. Note. NCAR/TN-282*.

Aucoin, F., D. Caissie, N. El-Jabi, and N. Turkkan, 2011: Flood frequency analyses for New Brunswick rivers. *Can. Tech. Rep. Fish. Aquat. Sci. 2920*, xi + 77p.

Beltaos, S., 2002: Effects of climate on mid-winter ice jams. *Hydrol. Process.*, **16**, 789–804, https://doi.org/10.1002/hyp.370.

Burrell, B. C., and J. E. Anderson, 1991: regional hydrology of new brunswick. *Can. water Resour. J.*, **16**, 317–330, https://doi.org/10.4296/cwrj1604317.

Caissie, D., and S. Robichaud, 2009: Towards a better understanding of the natural flow regimes and streamflow characteristics of rivers of the maritime provinces. *Can. Tech. Rep. Fish. Aquat. Sci.*, **2843**, 53.

Chen, C., and Coauthors, 2019: Themodynamic and dynamic Responses to deforestation in the maritime continent: a modeling study. *J. Clim.*, **32**, https://doi.org/10.1175/JCLI-D-18-0310.1.

Collins, M. J., J. P. Kirk, J. Pettit, A. T. Degaetano, M. S. McCown, T. C. Peterson, T. N. Means, and X. Zhang, 2014: Annual floods in new england (USA) and atlantic canada: Synoptic climatology and generating mechanisms. *Phys. Geogr.*, **35**, 195–219, https://doi.org/10.1080/02723646.2014.888510.

Dickinson, E., A. Henderson-Sellers, and J. Kennedy, 1993: Biosphere-atmosphere Transfer Scheme (BATS) Version 1e as Coupled to the NCAR Community Climate

Model. *NCAR Tech. Rep. NCAR/TN-3871STR*, *72*, 77.

El-Jabi, N., and D. Caissie, 2019: Characterization of natural and environmental flows in new brunswick, canada. *River Res. Appl.*, **35**, https://doi.org/10.1002/rra.3387.

Eljabi, N., D. Caissie, and N. Turkkan, 2015: Flood analysis and flood projection under climate change in New Brunswick. *Can. Water Resour. J. / Rev. Can. des ressources hydriques*, https://doi.org/10.1080/07011784.2015.1071205.

Farrar, J. L., 1995: *Trees in Canada*. Markham On. Fitzhenry and Whiteside Ltd.,.

Giorgi, F., and Coauthors, 2012: RegCM4: Model description and preliminary tests over multiple CORDEX domains. *Clim. Res.*, **52**, 7–29, https://doi.org/10.3354/cr01018.

Goeking, S. A., and D. G. Tarboton, 2020: Forests and water yield: A synthesis of disturbance effects on streamflow and snowpack in Western coniferous forests. *J. For.*, **118**, 172–192, https://doi.org/10.1093/jofore/fvz069.

Hibbert, A. R., 1967: Forest Treatment Effects on Water Yield. *Int. Symp. Hydrol.*, 527–543.

Kidd, S. D., R. A. Curry, and K. R. Munkittrick, 2011: *The Saint John River: A State of the Environment Report*. 175 pp.

Linke, J., Fortin, M.-J., Courtenay, S., Cormier, R., 2017. High-resolution global maps of 21st-century annual forest loss: Independent accuracy assessment and application in a temperate forest region of Atlantic Canada. *Remote Sens. Environ.*, **188**, 164–176.

Llopart, M., M. S. Reboita, E. Coppola, F. Giorgi, R. P. da Rocha, and D. O. De Souza, 2018: Land use change over the amazon forest and its impact on the local climate. *Water*, **10**, https://doi.org/10.3390/w10020149.

Lundberg, A., and S. Halldin, 2001: snow interception evaporation, review of measurments techniques, processes, and models. *Theor. Appl. Clim.*, **70**, 117–133, https://doi.org/10.1007/s007040170010.

Newton, B., and B. C. Burrell, 2015: The April–May 2008 flood event in the Saint John River Basin: Causes, assessment and damages. *Can. Water Resour. J. / Rev. Can. des ressources hydriques*, **41**, 118–128, https://doi.org/10.1080/07011784.2015.1009950.

Niu, X., J. Tang, S. Wang, and C. Fu, 2018: Impact of future land use and loand cover change on temperature projectionover east asis. *Clim. Dyn*, **52**, 6475–6490, https://doi.org/10.1007/s00382-018-4525-4.

Otieno, V. O., and R. O. Anyah, 2012: Effects of land use changes on climate in the Greater Horn of Africa. *Clim. Res.*, **52**, 77–95, https://doi.org/10.3354/cr01050.

Peel, M. C., B. L. Finlayson, and T. A. and McMahon, 2007: Updated world map of the Köppen-Geiger climate classification. *Hydrol. Earth Syst. Sci.*, **11**, 1633–1644, https://doi.org/10.5194/hess-11-1633-2007, 2007.

Reyes-González, A., J. Kjaersgaard, T. Trooien, D. G. Reta-Sánchez, J. I. Sánchez-Duarte, P. Preciado-Rangel, and M. Fortis-Hernández, 2019: Comparison of Leaf Area Index, Surface Temperature, and Actual Evapotranspiration Estimated Using the METRIC Model and In Situ Measurements. *Sensors*, **19**, 1857, https://doi.org/10.3390/s19081857.

Rokaya, P., S. Budhathoki, and K. E. Lindenschmidt, 2018: Trends in the Timing and Magnitude of Ice-Jam Floods in Canada. *Sci. Rep.*, **8**, 1–9, https://doi.org/10.1038/s41598-018-24057-z.

Stull, R. B., 1988: *An Introduction to Boundary Layer meteorology*. Kluwer Academic Publishers,.

Taylor, K. E., 2001: Summarizing multiple aspects of model performance in a single diagram. *J. Geophy. Res.*, **105**, 7183–7192.

Varhola, A., N. C. Coops, M. Weiler, and R. D. Moore, 2010: Forest canopy effects on snow accumulation and ablation: an intergrative review of empirical results. *j. Hydrol.*, **392**, 219–233, https://doi.org/10.1016/j.jhydrol.2010.08.009.

Yu, X., and C. P.-A. Bourque , 2022: Controls of contemporary (2001–2018) springtime waterflow dynamics in a large, snowmelt-dominated basin in northeastern North America. *J. Hydrol. X*, **14**, 100177. https://doi.org/10.1016/j.hydroa.2021.100117.

Zadeh, S. M., D. H. Burn, and N. OBrien, 2020: Detection of trends in flood magnitude and frequency in canada. *J. Hydrol. Region. Stud.*, **28**, https://doi.org//10.1016/j.ejrh.2020.100673.

Zahmatkesh, Z., S. K. Jha, P. Coulibaly, and T. Stadnyk, 2019: An overview of river flood forecasting procedures in canadian watersheds. *Can. Water Resour. Journal/Revue Can. des ressources hydriques*, https://doi.org/10.1080/07011784.2019.1601598.

Vita

Candidate's full name: Ahmed K. Shalaby

Universities attended:

2009–2013	Ph.D., Cairo University, Department of Astronomy and Meteorology.
2005–2007	M.Sc., Cairo University, Department of Astronomy and Meteorology.
2000–2001	Diploma in Meteorology, Cairo University, Department of Astronomy and Meteorology
1999–2000	World Meteorological Organisation (WMO) Class I, Egyptian Meteorological Authority, Cairo, Egypt.
1993–1997	B.Sc., Physics Major, Faculty of Science, Ain-Shams University, Cairo, Egypt.

Publications:

Ciarlo, J.M., Aquilina, N.J., Strada, S., **Shalaby, A.**, Solmon, F. 2021. A modified gas-phase scheme for advanced regional climate modelling with RegCM4. *Clim Dyn* **57,** 489–502. https://doi.org/10.1007/s00382-021-05722-y.

Salah, Z., **Shalaby, A.**, Steiner, A.L., Zakey, A.S., Guatam, R., Abdel Wahab, M.M. 2018. Study of aerosol direct and indirect effects and auto-conversion processes over the West African Monsoon region using a regional climate model, *Adv. Atmos. Sci.* doi:10.1007/s00376-017-7077-3.

Shalaby, A., Rappenglueck, B., Eltahir, E.A.B. 2015. The climatology of dust aerosol over the Arabian Peninsula, *Atmos. Chem. Phys. Discuss.*, 15, 1-49, doi:10.5194/acpd-15-1-2015.

Steiner, A.L., Tawfik, A.B., **Shalaby, A.**, Zakey, A.S., Abdel Wahab, M.M., Salah, Z., Solmon, F., Sillman, S., Zaveri, R.Z. 2014. Climatological simulation of ozone and atmospheric aerosols in the Greater Cairo region, *Clim. Res.*, doi:10.3354/cr01211.

Shalaby, A., Zakey, A.S., Tawfik, A.B., Solmon, F., Giorgi, F., Stordal, F., Sillman, S., Zaveri, R.A., Steiner, A.L., 2012. Implementation and evaluation of online gas-phase chemistry within a regional climate model (RegCM-CHEM4), *Geosci. Model Dev.*, 5,741–760.

Giorgi, F., Coppola, E., Solmon, F., Mariotti, L., Sylla, M.B., Elguindi, N., Diro, G.T., Nair, V., Guiliani, S., Cozzini, S., Guettler, I, O'Brien, T.A., Tawfik, A.B**.,** **Shalaby, A**., Zakey, A.S., Steiner, A.L., Stordal, F., Sloan, L.C., Brankovic, 2012. RegCM4: Model description and preliminary tests over multiple CORDEX domains, doi;10.3354/cr01018.

Rama Rao, Y.V., Hatwar, H.R., **Salah, A.K.**, Sudhakar, Y. 2007. An experiment using high resolution Eta and WRF models to forecast heavy precipitation over India, 164, 1593-1615, doi; 10.1007/s00024-007-0244-1.

Conference Presentations:

2014 May **Shalaby, A**. 2014. Severe dust storms over the Arabian Peninsula: observations and modeling, *Geophy. Res.* abstracts, Vol. 16, EGU2014-4965-1, EGU General Assembly.

2012 May Omar, M., Mahmoud, Z., Moustafa, S., **Shalaby, A**., Tawfik, A., 2012. RegCM4-Chem dust and gas-phase chemistry, Sixth ICTP Workshop on the Theory and Use of Regional Climate Models, presentation.

2010 May Fifth ICTP Workshop on the Theory and Use of Regional Climate Models (participant)

2009 April **Shalaby, A.**, Zakey, A. S., Giorgi, F., Solmon, F., 2009. Coupling of gas-phase chemistry to ICTP-Regional Climate Model (RegCM), *Geophy. Res.* Abstracts, Vol. 11, EGU2009-5506.

2008 May Forth ICTP Workshop on the Theory and Use of Regional Climate Models (participant).

2005 May Spring Colloquium on the Physics of Weather and Climate: Regional Weather Predictability and Modeling (participant)